Cerebrospinal Fluid Mechanics and Its Coupling to Cerebrovascular Dynamics

Andreas A. Linninger,[1,2] Kevin Tangen,[1] Chih-Yang Hsu,[1] and David Frim[3]

[1]Laboratory for Product and Process Design, Department of Bioengineering, University of Illinois at Chicago, Chicago, Illinois 60607; email: linninge@uic.edu

[2]Department of Neurosurgery, University of Illinois, Chicago, Illinois 60612

[3]Department of Neurosurgery, University of Chicago, Chicago, Illinois 60637

Annu. Rev. Fluid Mech. 2016. 48:219–57

First published online as a Review in Advance on August 28, 2015

The *Annual Review of Fluid Mechanics* is online at fluid.annualreviews.org

This article's doi: 10.1146/annurev-fluid-122414-034321

Keywords

CSF flow, intracranial dynamics, cerebral compliance, spinal compliance, porous brain tissue, intrathecal drug delivery

Abstract

Cerebrospinal fluid (CSF) is not stagnant but displays fascinating oscillatory flow patterns inside the ventricular system and reversing fluid exchange between the cranial vault and spinal compartment. This review provides an overview of the current knowledge of pulsatile CSF motion. Observations contradicting classical views about its bulk production and clearance are highlighted. A clinical account of diseases of abnormal CSF flow dynamics, including hydrocephalus, syringomyelia, Chiari malformation type 1, and pseudotumor cerebri, is also given. We survey medical imaging modalities used to observe intracranial dynamics in vivo. Additionally, we assess the state of the art in predictive models of CSF dynamics. The discussion addresses open questions regarding CSF dynamics as they relate to the understanding and management of diseases.

1. INTRODUCTION

Cerebrospinal fluid (CSF) fills the cerebral ventricles as well as the cranial and spinal subarachnoid spaces (SAS). An anatomical overview of the CSF-filled spaces is given in **Figure 1**. The enclosed fluid body is not static but exhibits pulsatile motion inside the ventricular system, and between the cranial vault and spinal compartments, superimposed by bulk flow due to fresh production and final clearance into the venous systems. The pulsatile pattern is essential to normal brain function, and several diseases manifest disturbances of CSF flow dynamics.

Recent efforts in the scientific and clinical communities aim at precisely quantifying critical parameters of normal intracranial dynamics as well as detecting characteristic deviations in diseases. Of special relevance is the intracranial pressure (ICP), which can be measured only invasively. Additionally, CSF flow velocities, brain motion, and deformations within the cranial and spinal compartments can be acquired noninvasively. In vivo medical imaging is providing an unprecedented window into intracranial and spinal dynamics. Image data help to precisely delineate patient-specific anatomical spaces, characterize blood and CSF flow, and trace the biodistribution of pharmacological drugs transported rapidly by pulsating CSF. Because in vivo imaging often provides only point measurements, researchers and clinical practitioners are forced to hypothesize about the biomechanical interactions between central nervous system (CNS) compartments. Unfortunately, conceptual ideas without quantitative verification have so far not solidified our understanding of brain disease enough to improve patient care.

Quantitative models are needed to provide hard predictions in support of new insights about the fluid dynamics of blood and CSF in the CNS. Judging by the growing body of publications reviewed in this article, mathematical modeling has already garnered the attention of the neurological surgery and neuroscience communities. There appears to be a growing consensus about the important role mathematical models can play for better interpretation of in vivo data acquired at multiple length scales and locations.

Mathematical models can be characterized by two extreme cases. In black box models, measurements are fitted against algebraic functions without considering the conservation principles that govern the flow. These black box models represent data but do not elucidate or interpret the physics of the transport phenomena. Although black box models reproduce data trends with high precision, they offer little insight into the functional role between parameters. Conversely, mechanistic models are rooted in fundamental conservation laws of mass, momentum, and chemical species. An increasingly important role is played by image-guided computational fluid dynamics (iCFD), which can simulate patient-specific scenarios for direct comparison to measurements in vivo (Linninger 2012). We advocate here the opinion that it is key for CFD models to avoid domains or limiting boundary conditions that diminish the rigorous computations to mere data fitting, but that they should explore novel hypotheses that account for the dynamic interaction

Figure 1

Anatomical diagram of the main structures in the central nervous system. The entire spinal and cranial space is shown on the left. (*a*) Detail of the cranial SAS (*light blue*), the four ventricular spaces (*blue*), and brain parenchyma (*pink*). Also shown is the location of the choroid plexus (*green*) inside the ventricles and arachnoid villi (*red*) at the superior most aspect of the cranial space. (*b*) Magnification of the cortical surface illustrating the penetrating arterioles, surrounding perivascular space, underlying pia mater and glia limitans. Panel *b* adapted from Iadecola & Nedergaard (2007) and Louveau et al. (2015). (*c*) Depiction of the spinal SAS at the lower thoracic region, T8–T12. The spinal cord is colored in yellow. Nerve roots protrude from the spinal cord and exit the dura membrane (*gray envelope*). Arachnoid trabeculae (*dark blue*) are microscopic features below the threshold for imaging but are illustrated here for context. (*d*) An axial plane highlighting the orientation of nerve roots (*yellow*) at the thoractic T10 inside the spinal SAS (*blue*). (*e*) An axial plane of the spinal SAS and spinal cord structures: spinal cord gray matter (*dark yellow*) and white matter (*yellow*). The three meningeal layers dura (*brown*), arachnoid (*dark blue*), and pia membrane (*purple*) are indicated. Arachnoid trabeculae are shown as thin dark blue lines. Abbreviations: CSF, cerebrospinal fluid; SAS, subarachnoid spaces.

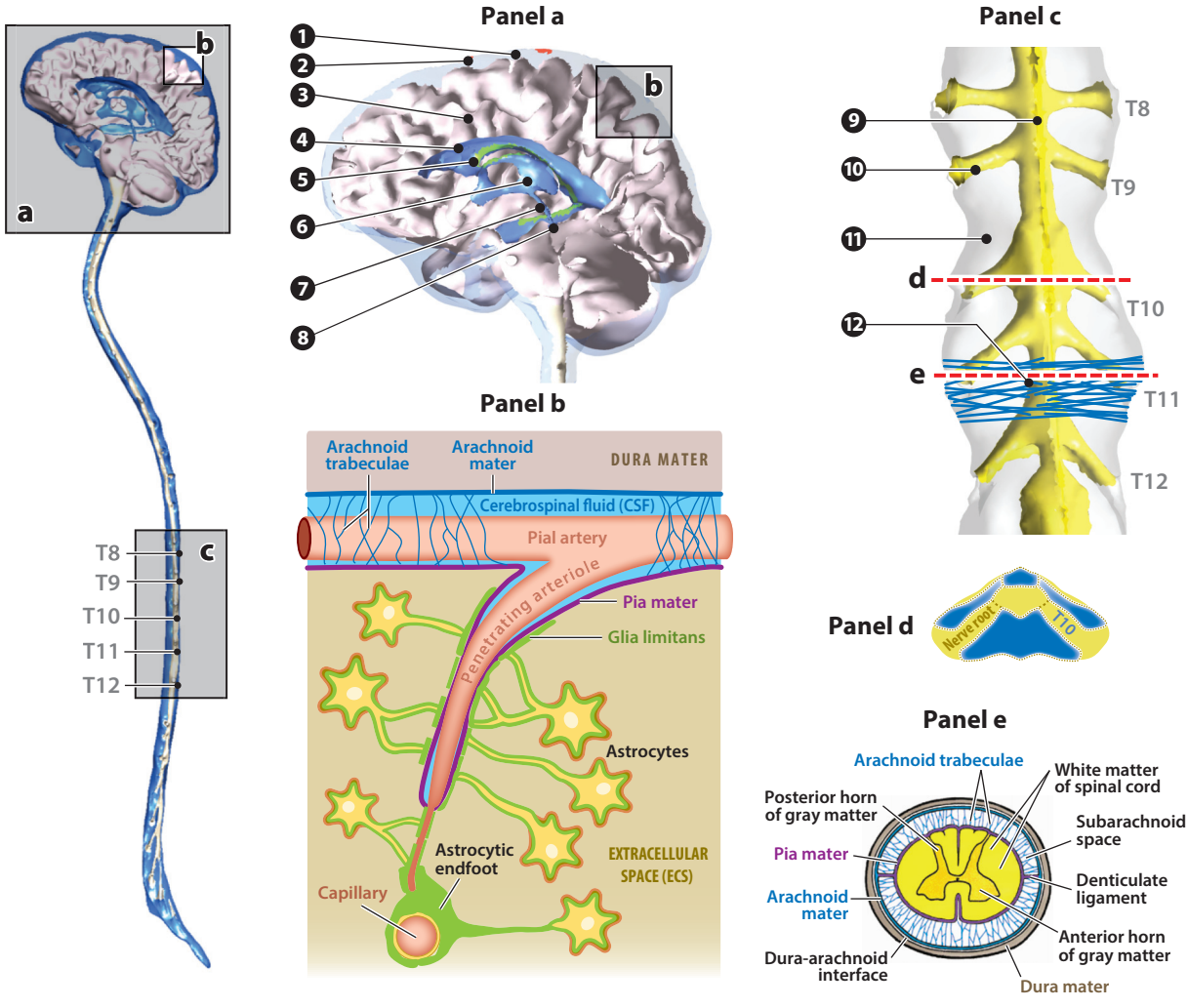

ITEM	DESCRIPTION	ITEM	DESCRIPTION
1 Cranial SAS	CSF-filled space between pia and arachnoid mater in cranium	7 Aqueduct	Connects the third and fourth ventricles in the brain
2 Villi	Extension of arachnoid into venous sinus; possible site of CSF drainage	8 Fourth ventricle	CSF-filled cavity; ventricle can drain into spinal SAS
3 Paren-chyma	Brain tissue composed mainly of neuronal and glial cells	9 Spinal cord	Nerve cells connecting central and peripheral nervous system
4 Lateral ventricle	CSF-filled cavity in both hemispheres of the brain	10 Nerve root	Extension of nerve bundles leaving central nervous system at T8–T12
5 Choroid plexus	Ependymal cells lining sections of all ventricles; site of CSF production	11 Spinal SAS	CSF filled space between pia and arachnoid membrane in the spine
6 Third ventricle	CSF-filled cavity on midline of brain between lateral ventricles	12 Trabeculae	Microscopic projections between arachnoid and pia mater

of all major CNS compartments. Motivated by these considerations, this review is organized around three key topics given their significance: (*a*) diseases of CSF dynamics, (*b*) medical imaging techniques to visualize flow, and (*c*) mathematical models to predict normal and disease conditions.

Section 2 begins with a current view of intracranial dynamics relating the CSF flow to vascular pulsations. We discuss contradictory evidence regarding bulk flow. Section 3 provides an account of diseases of CSF dynamics, covering hydrocephalus, syringomyelia, Chiari malformation type 1 (CM1), and pseudotumor cerebri (PTC). Section 4 highlights medical imaging techniques to observe CSF and blood motion in vivo. Section 5 provides an overview of mathematical models of CSF dynamics. We review compartmental models, detailed models of intracranial dynamics and spinal fluid flow, and models of CSF flow in the entire CNS. Section 6 critically assesses the state of the art. Section 7 concludes with a perspective for future research directions.

2. BACKGROUND ON PHYSIOLOGICAL INTRACRANIAL DYNAMICS

2.1. Cerebrospinal Fluid Motion in the Cranium

The brain and spinal cord are surrounded by CSF, a clear fluid with a density and viscosity close to water. Its protein content is lower than that of blood plasma (Sakka et al. 2011). It fills the ventricular system and the cranial and spinal SAS. CSF inside the CNS does not remain stagnant but pulsates through the lateral ventricles. Imaging studies have confirmed that the cardiac cycle imposes its pulsatile pattern onto the CSF (Enzmann & Pelc 1993). CSF also flows from the cranial to the spinal SAS in systole, with flow reversal from the spinal SAS into the cranium in diastole. A respiratory influence on the CSF oscillations in the aqueduct has also been observed (Bhadelia et al. 2013, Dreha-Kulaczewski et al. 2015, Kao et al. 2008, Schroth & Klose 1992, Williams 1981, Yamada et al. 2013).

In addition to the marked flow oscillations with no net flux, there is evidence of a small volumetric bulk component. Fresh CSF is believed to be secreted through the epithelium of the choroid plexus (**Figure 1**). **Figure 1*a*** shows the two lateral ventricles communicate with the third ventricle, and a thin tubular channel, the aqueduct of Sylvius, connects the third to the fourth ventricle. Aqueductal flow exhibits strong pulsatility (Wagshul et al. 2011). The foramina of Magendie and Luschka exit the fourth ventricle into the cerebral SAS at the prepontine area. Because the human CNS lacks a classical lymphatic system, CSF clearance differs from peripheral extracellular fluid drainage. CSF is believed to be reabsorbed into the venous system through the arachnoid villi, protrusions of the arachnoid membrane into the superior sagittal sinus, located at the top of the head (**Figure 1*a***) or alternatively through nerve paths into the extracranial lymphatic system. Animal experiments suggest that lymphatic drainage is significant in rodents (Boulton et al. 1999, Kida et al. 1993) and dogs (Leeds et al. 1989, Mao et al. 2010). Recent findings point toward the existence of a meningeal lymphatic network in mice (Louveau et al. 2015). However, the extent of lymphatic drainage in humans is still debated (Johnston et al. 2004, Wagshul & Johnston 2013). Alternative theories of CSF production and reabsorption question this traditional view (Bulat et al. 2008, Bulat & Klarica 2011, Klarica et al. 2005, 2013; Orešković & Klarica 2011). Supported by dilution experiments in cats, Klarica et al. (2005) proposed the theory that CSF production and reabsorption occur throughout the parenchyma without a clear bulk component due to choroidal production or clearance through arachnoid villi.

2.2. Intercellular Fluid Inside the Interstitium

The traditional view also holds that a fraction of CSF is secreted from the brain tissue, in agreement with Klarica et al.'s theory (Cserr 1971, Milhorat 1969, Milhorat et al. 1971). Intercellular fluid

(ICF) originating inside the brain percolates through the tortuous extracellular space (ECS) into the ventricles. ICF transport from inside the parenchyma to the cranial SAS through the pial membrane (**Figure 1*b***) is also possible in principle but has not been verified experimentally. The classical view of the brain as a sponge (Hakim 1970, Hakim et al. 1976, Penn & Bacus 1984) has prompted applications of porous media theory to the biomechanics of the brain (Narsilio et al. 2008, Smith & Humphrey 2007, Tully & Ventikos 2009, Vardakis et al. 2013). Beyond the limited concept of the brain tissue acting as a passive sponge, new data suggest that the brain actively regulates the size of the ECS in accordance with metabolic needs (Iadecola & Nedergaard 2007). In addition to the possibility of fluid generation inside the tissue, ICF reabsorption from the interstitium into the microvasculature has been proposed as a way to interpret brain water content changes (Penn & Bacus 1984, Penn & Kurtz 1977). Experimental evidence also suggests the notion of net flow of CSF into the interstitial brain tissue (Penn et al. 2009, 2011). Several studies show that CSF can exit the ventricles under high pressure (Hodel et al. 2013, Lebret et al. 2013, Sæhle & Eide 2015). Transependymal flow into perivascular spaces may be significant in hydrocephalus (Hopkins et al. 1977). The role of osmolarity exercising Starling forces needs to be quantified to determine the amount and directionality of bulk water exchange across the blood-brain barrier (Buishas et al. 2014). Water exchange from astrocytic endfeet (**Figure 1*b***) into the ECS sparked a growing interest in transmembrane proteins known as aquaporin channels (Haj-Yasein et al. 2011, MacAulay & Zeuthen 2010, Nedergaard et al. 2003, Papadopoulos & Verkman 2013, Zeuthen 2010). Despite these developments, a high degree of uncertainty about the amount, direction, and physiochemical driving forces of interstitial fluid exchange remains.

2.3. Perivascular Intercellular Fluid Transport and Cerebral Lymphatics

Distinct and apart from extracellular movement of ICF, perivascular tracer transport experiments suggest a separate fluid conduit along arteries (Carare et al. 2008, Hadaczek et al. 2006, Hutchings & Weller 1986, Iliff et al. 2012, Schley et al. 2006). Arterial walls encompass a fluid-filled perivascular space between the leptomeninges and the endothelium (**Figure 1*b***) (Weller et al. 1992, Zhang et al. 1990). It has been speculated that systolic arterial expansion also drives pulsatile motion in perivascular spaces (Iliff et al. 2013), but actual volumetric flow rates of ICF flux in the perivascular space have so far not been quantified.

2.4. Cerebrospinal Fluid Inside the Spinal Compartment

The textbook picture of meandering CSF flow along the spinal canal is obsolete (Bering 1952, Greitz 2004), giving way to flow patterns derived from flow velocity measurements acquired in vivo with cine phase-contrast magnetic resonance imaging (PC MRI). In normal humans, 1–2 mL of CSF are displaced into the cervical SAS during systole in each cardiac cycle and flow back into the cranial SAS during diastole. Four-dimensional (4D) magnetic resonance measurements show a sharp CSF pulse shooting from the prepontine area into the cervical SAS (Bunck et al. 2012). Additionally, flow velocities are higher in the anterior cervical SAS, with concentrated jets propagating along the cervical region. Enzmann & Pelc (1992) also examined brain and spinal cord motion in healthy subjects, recording caudal displacements up to 0.5 mm following carotid systole. They observed tissue motion, suggesting that the entire brain and spinal cord slightly move up and down in each cardiac cycle.

Craniocaudal flow into the spinal SAS requires concomitant expansions of the fluid-filled spaces. The systolic CSF inflow into the spinal SAS is believed to be accommodated by the deformation of the dura membrane, which in turn is enabled by displacement of venous blood or

the compression of fatty epidural tissue especially in the lumbar region (Marmarou et al. 1975, Shapiro et al. 1980). PC MRI velocity measurements depict a gradual decline in the CSF stroke volume when measured at descending locations from the cervical to the lumbar spine. In addition to volumetric flow rate peak amplitude attenuation, a gradual increment in the phase lag of the velocity maximum was observed (Wagshul et al. 2006). Measured peak amplitude attenuation and phase lags were used to infer the volumetric strains responsible for spinal compliance (Tangen et al. 2015). More precise measurements of the velocity waves and their timing are expected to localize and quantify the spatial extent of spinal dura deformations.

The spinal CSF flow experiences intricate geometry-induced microflow patterns due to microanatomical aspects that can be found in the SAS (**Figure 1*c–e***). Microanatomical features causing complex flows include ligaments, nerve roots, trabeculae, meningeal layers, and spinal white matter and gray matter, which have been carefully characterized by Reina et al. (2002a,b, 2004, 2015). Several groups are beginning to clarify the role of nerve roots on the geometry-induced CSF flow patterns in the spine (Hettiarachchi et al. 2011, Pahlavian et al. 2014, Stockman 2005, Tangen et al. 2015).

The interaction of CSF with the spinal arteries has been studied by Bilston et al. (2003, 2009). The possible reabsorption of CSF in the spinal canal has also been investigated (Brodbelt & Stoodley 2007, Edsbagge et al. 2004, Lorenzo et al. 2015). To date, it appears that the spinal cord is not a major site for CSF clearance.

2.5. Coupling Between Cerebrospinal Fluid Flow and Cerebral Vasculature

As stated above, the CSF bulk flow due to fresh production and reabsorption is small compared to its pulsatile component. Pulsatile CSF oscillations are believed to be driven by systolic vascular dilatation followed by diastolic contraction. Recently, ependymal cilia lining the cerebral ventricles were shown to influence near-wall CSF flow in mice (Lechtreck et al. 2008, Siyahhan et al. 2014). To better understand the spatial distribution of the blood-CSF interaction, we briefly give an account of the cerebral angioarchitecture next.

2.5.1. Cerebral angioarchitecture. **Figure 2** provides an overview of the cerebral angioarchitecture. Most of the arterial blood enters the brain through large arteries, which include the internal carotid as well as two vertebral arteries, which join into the basilar artery. The internal carotid and basilar arteries discharge into a ring-like structure known as the circle of Willis, which distributes the cerebral blood flow to three major cerebral arteries in each hemisphere—the anterior cerebral artery (ACA), middle cerebral artery (MCA), and posterior cerebral artery (PCA)—each one supplying a different territory of the cerebral cortex (**Figure 2**). The largest blood volume enters through the MCA, supplying the parietal lobe and arteries leading to the choroid plexus, the major site of CSF secretion. The ACA delivers blood to the frontal lobe and cortical surfaces separating the cerebral hemispheres (Sylvian and longitudinal fissures). The PCA perfuses the occipital lobe. The cerebellum is supplied by the side branches of the basilar artery. The main segments of the ACA, MCA, and PCA branch into smaller vessels along the cortical surface. The microcirculatory blood supply to the deep cortical layers is described elsewhere (Linninger et al. 2013).

2.5.2. Force interactions. During the normal cardiac cycle, approximately 750 mL of blood are pumped into the head per minute. The systolic pressure rise inflates arterial blood vessels, thus augmenting the cerebral blood volume during systole. Because the cranial vault is enclosed by ossified bone in adults, the vascular expansion of the main arteries traversing CSF-filled spaces triggers CSF displacement. MRI evidence suggests that the total cerebral blood volume inflates

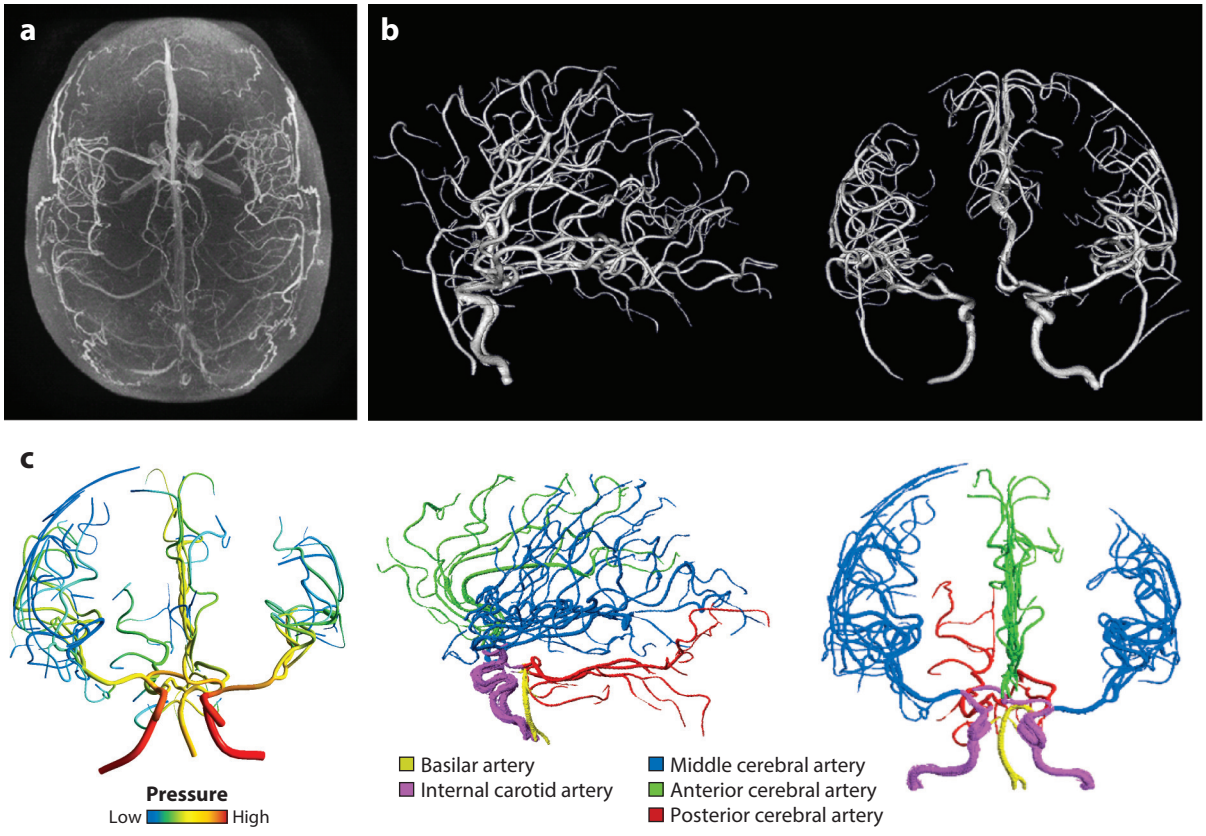

Figure 2

Overview of the human cerebral angioarchitecture reconstructed from subject-specific medical images. (*a*) Magnetic resonance angiography capturing the unique features of the vascular tree of a 29-year-old volunteer. (*b*) Subject-specific surface meshes extracted from raw image data through image filtering and reconstruction techniques. Panel *b* adapted from Hsu et al. (2015). (*c*) Rigorous subject-specific 3D CFD simulation showing the pressure distribution of blood flow through a large portion of the arterial tree. The massive simulation was made possible by the use of parametric meshes as described in Ghaffari et al. (2015). The symbol key indicates the territories of the main cerebral arteries.

and deflates in each cardiac cycle by approximately 1–2 mL, the same volumetric amount as there is CSF exchange between the cranial and spinal SAS (Freund et al. 2001).

In addition to pulsations of the main arteries running along the cortical surface, smaller penetrating arterioles or the capillary bed, both of which are embedded inside the cortical tissue, may also distend. Volumetric dilatation of the microcirculatory structures would need to be transmitted to the surrounding parenchyma. Brain tissue dilation would in turn have to displace ICF through the ECS into the ventricular system or produce brain motion, as observed by Enzmann & Pelc (1992, 1993).

An MRI technique developed by Zhu et al. (2006) permitted the quantification of ventricular wall motion, which propels CSF flow inside the ventricular system. Two effects might be at work: For example, vascular volume dilatation could be transmitted from the cortical surface through brain tissue, whose compression causes ventricular space contraction. Alternatively, ventricular wall motion could arise from inside the ventricles by systolic expansion of the choroidal arteries,

such that ventricular walls pulsate against the periventricular ependymal layer. Ventricular dilation due to choroid expansion was hypothesized in the theoretical model of Linninger et al. (2005) and measured with cine PC MRI (Zhu et al. 2006).

Alternatively, modest brain compression could be accommodated by ECS reduction. In this case, continuity demands an exit route for displaced ICF. For this scenario, two routes come to mind: (*a*) the displacement of ICF into the ventricles or (*b*) ICF reabsorption into the capillary bed. However, water shifts from the ECS to the capillary bed are opposed by strong Starling forces, so the bulk fluid exchange should be quite limited (Buishas et al. 2014).

In addition to arterial expansion, the compression of the venous system under high pressure has been hypothesized, which would lead to cross-sectional area deformation, reduction in venous blood lumen, or even collapse of sections of the venous tree. Greitz et al. (1994) speculated that the venous system is compressible, especially in patients with high ICP. Accordingly, high ICPs compress the venous bed mainly in the superior sagittal sinuses (for anatomical details, see **Figure 2**). Diminished venous lumen induces feedback that lowers blood flow owing to the hike in resistance. The possible collapse of vertebral blood flow when the ICP exceeds 30 mmHg, as well as reduced blood flow occurring in benign cerebral hypertension, supports the notion of a compressible or collapsible venous bed (Auer & Ishiyama 1986, Bouma et al. 1992, Yada et al. 1973). Abnormal CSF flow is prominent in diseases of the CSF, as described next.

3. DISEASES OF CEREBROSPINAL FLUID DYNAMICS

There are several prominent disease states that represent dyscrasias of CSF dynamics. Some are based on the straightforward situation of CSF flow obstruction, although there are nuances even to that simple case. Others are more complicated and entail effects of CSF pulsatility or the viscoelastic properties of the brain. We summarize below several of the most common syndromes of abnormal CSF flow dynamics, including clinical manifestations, diagnosis, and management. An overview of anatomical changes in these diseases is provided in **Figure 3**. Current open research questions regarding each disease are also mentioned.

3.1. Hydrocephalus

Hydrocephalus occurs at an incidence of 1:1,000 to 1:500 in the general population in the United States. It results from an inappropriate volume of CSF in the cerebral ventricles at an inappropriate pressure. This definition describes nearly all situations that are commonly considered hydrocephalus yet excludes other entities, such as PTC (discussed in Section 3.4). The clinical manifestations of hydrocephalus reflect symptoms of increased ICP. This primarily includes headache and altered mental status. Signs that can be elicited by neurological examination include papilledema, defects in upgaze due to the enlargement of the third ventricle, balance loss, cognitive loss, and reduced short-term memory (Friedman & Jacobson 2002, Hebb & Cusimano 2001, Vanneste 2000, Williams et al. 2007). In children, hydrocephalus can lead to enlarged head size; in the elderly, loss of bladder control can be seen.

The imaging hallmark of hydrocephalus is the enlargement of the cerebral ventricles, with evidence of inappropriately elevated pressure in the ventricles demonstrated by transependymal flow of CSF into the periventricular tissues (Hopkins et al. 1977, Leliefeld et al. 2009, Zimmerman et al. 1986). In some cases, increases in the ventricular volume can be subtle. Research efforts in hydrocephalus imaging have recently been centered on automated algorithms for determining changes in the ventricular volume, as well as other imaging modalities that can demonstrate CSF

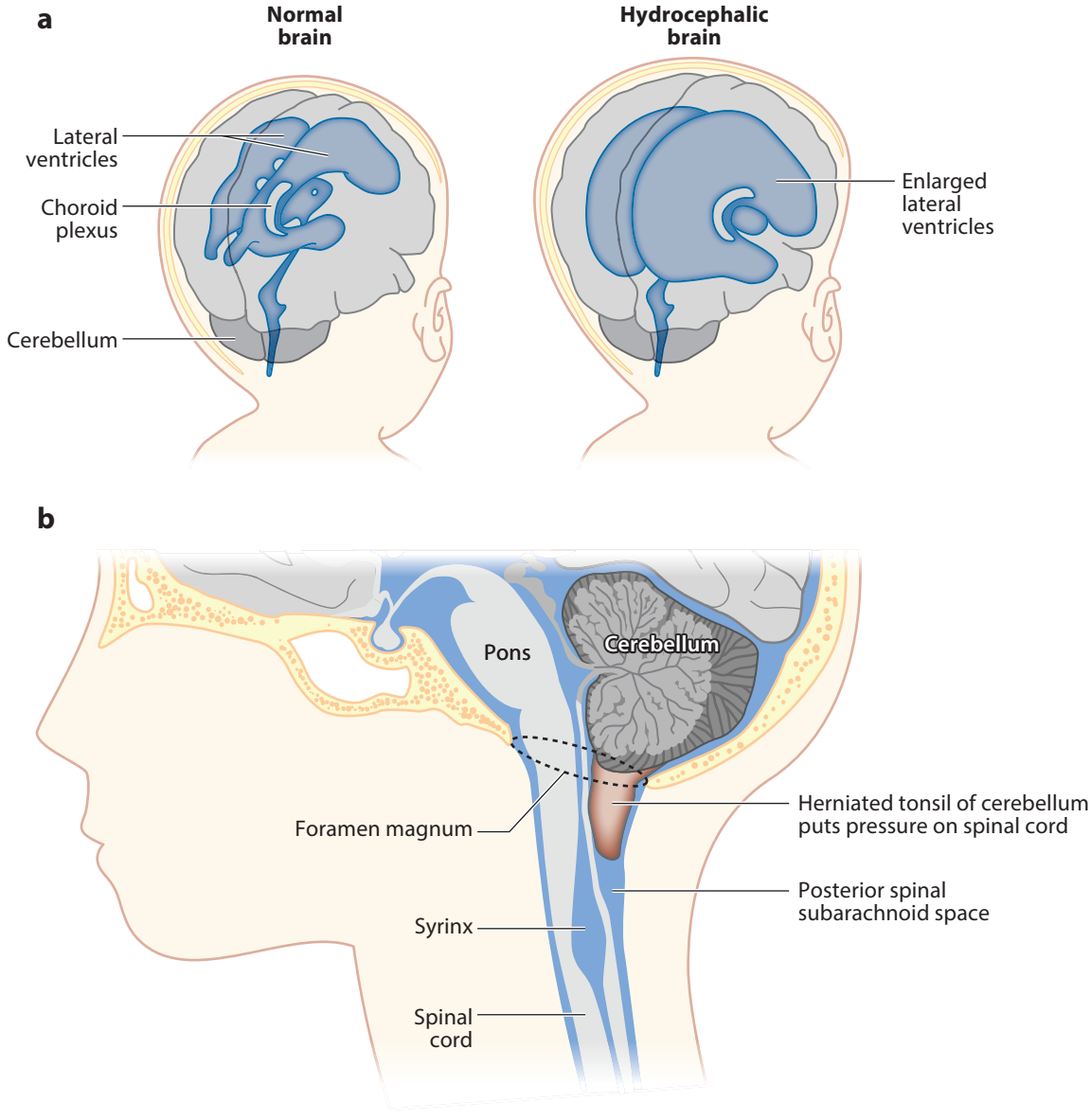

Figure 3

Overview of anatomical changes in diseases of intracranial dynamics. (*a*) Hydrocephalus is characterized by fluid accumulation in the brain leading to ventricular enlargement. A normal brain (*left*) is compared to a hydrocephalic brain (*right*) with increased lateral ventricles. Panel *a* adapted courtesy of Laboratory of Implantable Microsystems Research. (*b*) Chiari malformation is the result of herniated cerebellar tonsils that distend into the foramen magnum, obstructing the posterior spinal subarachnoid space. Syringomyelia is associated with the formation of a syrinx, a fluid-filled cavity in the spinal cord. Panel *b* adapted courtesy of Children's Neurological Associates.

seeking to escape the ventricular system under high pressure (Ambarki et al. 2012; Hodel et al. 2012, 2013; Ishii et al. 2013; Lebret et al. 2013; Sæhle & Eide 2015).

The pathophysiology of hydrocephalus is one of either direct obstruction, such as the situation of aqueduct obstruction, or primary malabsorption of CSF. Treatment of obstruction is through the removal of the obstructing lesion or through an internal or external bypass of the obstruction that restores normal CSF flow. The most common cause of hydrocephalus is malabsorption of the CSF at the level of the arachnoid villi, often after intraventricular hemorrhage of blood into the ventricles in a newborn, which is treated by shunting of the CSF to an extracranial reabsorptive surface. These approaches have proven to be lifesaving in a disease that as few as 65 years ago was uniformly fatal. However, the CSF flow dynamics found after treatment are hard to describe and are not identical to those found in the normal state. Rigorous fluid dynamic modeling of both the normal and hydrocephalic state within the ventricles and the SAS (e.g., **Table 1**) will greatly assist the design of internal bypass strategies to normalize CSF flow in the setting of obstructive hydrocephalus. In addition, modeling the nuances of normal CSF flow throughout the ventricular system to its absorptive surface will greatly inform the design of shunting devices that aim to restore the CSF dynamics of the normal state. The reconstitution of normal CSF dynamics in the setting of hydrocephalus represents a fundamental knowledge gap in the treatment of hydrocephalus; however, that gap will not be bridged until significant progress is made in the understanding of ventricular CSF secretion, circulation, and reabsorption. The contributions that can be expected from mathematical models are discussed in Section 5.

3.2. Chiari Malformation Type 1

The Chiari malformations were described in the early 1890s by Hans Chiari in stillborn children with hindbrain abnormalities. Although four malformations were described, they are unrelated except for their anatomic location in the posterior fossa and their involvement with the cerebellum and brainstem. CM1 is the least complicated of those malformations, although it is accompanied by a clinical syndrome that is the least understood. A simple definition of CM1 is the extension of the cerebellar tonsils below the level of the foramen magnum into the cervical SAS. The herniation of the cerebellar tonsils outside of the cranial vault disrupts CSF flow in a variety of ways, from frank obstruction of CSF flow out of the foramen of Magendie to subtle decreases in both the flow and pulsatility of the CSF within the cranial vault. Anatomical positions and disease characteristics are shown in **Figure 3**. In this situation, various symptoms can occur, although their specific etiological bases are poorly understood.

The hallmark clinical syndrome that accompanies CM1 is an occipital headache that occurs with tussive maneuvers, including coughing or sneezing. Other symptoms can include chronic headache, pain, or other sensory changes in the nape of the neck, the shoulders, or the upper extremities (George & Higginbotham 2011, Nash et al. 2001). Symptoms related to compression of the brainstem in the posterior fossa include dysphagia, apnea, syncope during times of exertion (termed a Chiari dropping attack), and the presence of a syrinx, as described in Section 3.3. How these symptoms relate to the cerebellar herniation and other classical manifestations of this syndrome, which can include a decrease in the size of the posterior fossa and other bony abnormalities, remains elusive. The incidence of CM1 in the population is estimated at approximately 1:1,200 in the United States. In general, the belief among clinicians is that the majority of people born with cerebellar tonsillar herniation are asymptomatic. The hallmark of the diagnosis of CM1 is MRI of the cerebellar tonsils and the posterior fossa showing tonsillar herniation without any other anatomical abnormalities of the brain. Initial management of CM1 is medical treatment of sensory symptoms such as headache or painful paresthesia. There is no specific medical treatment for the

Table 1 Compilation of studies on abnormal CSF dynamics in CNS diseases

Reference	Description
Hydrocephalus	
Balédent et al. (2004)	Used MRI to measure cerebral blood and CSF flow in communicating HC and healthy subjects. Found increase in CSF ventricle flush in HC patients due to venous compression.
Linninger et al. (2005)	Used a fluid-structure interaction model of ventricular CSF spaces to predict flow, pressure values, and parenchyma deformation. Canine experiments measured pressure and found no transmural pressure gradients for hydrocephalic animals.
Linninger et al. (2007)	Measured CSF velocity by MRI in healthy and HC patients. Reconstructed 3D models and simulated CSF flow and ICP increase in HC patients.
Petrella et al. (2008)	Measured CSF parameters before and after shunting for normal NPH patients. Performed infusion studies to investigate compliance reserve.
Linninger et al. (2009b)	Dynamically predicted realistic phase lags between the arterial and venous blood vessels, and CSF motion in the ventricles with oscillatory CSF displacement between cranial and spinal SAS. Demonstrated a measured and predicted increase of aqueduct CSF pulsatility and lower prepontine flows in HC compared to normal patients.
Tully & Ventikos (2009)	Coupled poroelastic and CFD solvers to model effect of aqueduct stenosis on ventricular dilation with pulsatile flow. Predicted pressure drop and magnitude of tissue dilation.
Sweetman et al. (2011)	With cine PC MRI, measured CSF velocity in ventricular system for normal and HC patients. Velocity measurements validated model predictions. Predicted small transmantle pressure gradients.
Qvarlander et al. (2013)	Examined CSF dynamics in normal pressure hydrocephalus, specifically the pulse amplitude of the ICP pulsations during a compliance test. Concluded that pulsatility and compliance changes are primary aspects governing CSF dynamics in hydrocephalus.
Chiari malformation type 1	
Armonda et al. (1994)	Imaged Chiari and surgical revision patients with cine MRI. Demonstrated that tonsillar herniation obstructed CSF flow, decreased velocity, and reduced caudal flow duration compared to normal subjects. Postsurgical CSF flow parameters returned to control levels.
McGirt et al. (2005)	Measured CSF flow in Chiari patients with incidence of headache. Found that occipital headaches have tenfold greater incidence of obstructed CSF flow and eightfold greater occurrence of tonsillar descent than frontal/general headaches.
Shah et al. (2011)	Conducted an expanded MRI study of Chiari patients from the craniovertebral junction to include upper cervical SAS due to CFD predictions of increased CSF velocity. Peak velocity measured at C4 spine.
Rutkowska et al. (2012)	Measured CSF velocity in the cervical SAS by MRI for Chiari patients, craniovertebral decompression patients, and healthy subjects. CFD simulations performed on reconstructed models predicted higher velocity for Chiari patients, which returned to control levels following surgery. This is in good agreement with MRI.
Cousins & Haughton (2009)	Compared cerebellar tonsil motion in healthy subjects with Chiari patients and found that pathological cases have 33% larger extent of movement, values ranging from 0.43 to 0.61 mm.
Pahlavian et al. (2014)	Imaged normal and diseased subjects with MRI for reconstruction of SAS with 4D MRI flow measurements. CFD simulation performed with and without microanatomical structures' concluded that microanatomical structures lead to formation of vortices facilitating mixture of CSF.

(*Continued*)

Table 1 (*Continued*)

Reference	Description
Syringomyelia	
Chang & Nakagawa (2003)	Studied wave propagation along spine using electric circuit model of CSF spaces. Hypothesized that the cisterna magna acts as a shock absorber; therefore, reduced CSF space by tonsillar herniation leads to syrinx formation.
Martin et al. (2005)	Reconstructed an in vitro model using MRI to examine the hydrodynamics of SAS with syringomyelia.
Struck & Haughton (2009)	Measured CSF velocity at foramen magnum in patients with IS. Found that IS patients presented with increased peak systolic CSF velocities and flow jets.
Koyanagi & Houkin (2010)	Reviewed theories and evidence of syrinx formation. Proposed that, in addition to CSF flow mechanisms, lower extracellular fluid adsorption as a function of reduced spinal vein and spinal SAS compliance can lead to syrinx formation.
Bilston et al. (2009)	Utilized a CFD model to predict impact of spinal arterial pulse wave timing and CSF pressure on CSF flow. Indicated that pressure wave timing influences CSF flow from SAS to PVS.
PTC	
Karahalios et al. (1996)	Observed 10 PTC patients (five with dural venous outflow obstruction and with five normal outflow). Found that all pressure measurements were elevated.
Levine (2000)	Proposed a cranial model of porous parenchyma containing blood vessels, an internal ventricular cavity, and cranial SAS to test PTC and CSF adsorption.

Abbreviations: CFD, computational fluid dynamics; CNS, central nervous system; CSF, cerebrospinal fluid; HC, hydrocephalic; ICP, intracranial pressure; IS, idiopathic syringomyelia; MRI, magnetic resonance imaging; NPH, normal pressure hydrocephalus; PC MRI, phase-contrast magnetic resonance imaging; PTC, psuedotumor cerebri; PVS, periventricular space; SAS, subarachnoid spaces.

problems of apnea, aspiration, or Chiari dropping attacks, all of which constitute indications for surgical treatment. The surgical treatment of CM1 generally includes a bony decompression or enlargement of the posterior fossa, which is often accompanied by an expansive duraplasty for further enlargement of the craniocervical junction SAS. Many surgeons who commonly treat Chiari malformations will also explore the SAS at the level of the foramen magnum to ascertain that CSF flow out of the fourth ventricle is unimpeded by the cerebellar tonsils, by any other arachnoid scarring, or by the presence of a retained rhomboid roof (see **Figure 3**).

Many models of the normal flow of CSF in and around the foramen of Magendie and the foramen magnum have been developed to explain the abnormal CSF dynamics found in symptomatic CM1 (see **Table 1**). None of these models as yet has been fully satisfying in explaining the abnormality. That being said, as the modeling of this CSF dyscrasia becomes more sophisticated, that data will better inform the choice of treatment based on individual patient manifestations of the CSF flow disturbances. This begs the question of how normality can be restored to CSF dynamics at the skull base without a clear understanding of these dynamics in the normal state.

3.3. Syringomyelia

Syringomyelia has been defined in several ways over many decades. One durable definition has been a dilatation of the central canal of the spinal cord owing to obstruction of flow within the spinal cord or the surrounding SAS (**Figure 3**). Given its simplicity, this definition neglects the ongoing debate regarding the dynamics of CSF production and flow dynamics in the spinal cord under normal circumstances (Hladky & Barrand 2014). The incidence of syringomyelia is unknown in the population as it is most commonly associated with Chiari malformations although

is also associated with trauma to the spinal cord, tumors of the spinal cord, or an idiopathic state with no demonstrable cause. The clinical presentation of syringomyelia is that of an expansile mass within the spinal cord that is centrally located (Aubin et al. 1981, Cahan & Bentson 1982). The syrinx can cause the stretching of sensory fibers located near the central canal, leading to a pain syndrome or numbness. As the fluid within the spinal cord expands, further spinal cord malfunction occurs, which can affect motor function below the level of the lesion.

The management of syringomyelia is generally surgical and includes an approach to correcting the etiology of the syrinx, decompression of CM1 for Chiari-associated syrinx, or the removal of a CSF-obstructing spinal cord tumor. The specifics of the CSF dynamics that lead to the formation of a syrinx in any of the etiological settings mentioned above are still not entirely understood. It is this lack of understanding that hampers the design and implementation of uniformly successful surgical approaches. Oftentimes, the restoration of a patent SAS in a syringomyelic segment of the spinal cord will resolve the syrinx. Decompression surgery of CM1 that is associated with a syrinx is the most reliable treatment for Chiari-associated syringomyelia, although the specifics of what aspect of the Chiari decompression leads to syrinx resolution are not agreed on. Free outflow of CSF through the foramen of Magendie or changes in the CSF pressure gradient in and around the cisterna magna have been suggested. Both theoretical and mechanical models of syringomyelia have been constructed, as seen in the examples in **Table 1**. Through these models, it is possible to predict some factors that might lead to syrinx formation. However, there still remains a knowledge gap between current models and the physiological situation found in a symptomatic syrinx. Open research questions regarding syrinx are similar to those described in nearly all of the CSF clinical dyscrasias: How can an abnormal state of CSF dynamics be modeled when so little is known about the normal state?

3.4. Pseudotumor Cerebri, Idiopathic Intracranial Hypertension, and Benign Intracranial Hypertension

Pseudotumor cerebri (PTC), also known as idiopathic intracranial hypertension and benign intracranial hypertension, is a syndrome with symptoms that include headache, elevated CSF pressure, and other manifestations of increased ICP, including papilledema. This syndrome was described before any sophisticated imaging of the nervous system existed, and its name is based on the expectation of a tumor within the cranial vault causing increased pressure; when no lesion was found, the term pseudotumor was applied. Although now obsolete, this name is applied to a variety of situations of idiopathic increases in CSF pressure without mass lesion, obstruction, or increase in the size of the ventricles.

The clinical manifestations of this syndrome include headache, visual disturbances, and no specific abnormality on brain or spine imaging. Management of the syndrome generally includes treatment of the cause (if known), such as obesity, or medical reduction in CSF production through the use of diuretics (Johnson et al. 1998). Failure of medical management leads to the use of a CSF shunting device that mechanically lowers the CSF pressures, relieving the symptoms, which are related entirely to the elevated CSF pressure. However, placement and maintenance of the shunting devices within the context of the very obese can be quite difficult. Oftentimes the syndrome in the morbidly obese is not treatable. The specific nuances of CSF dynamics that lead to PTC are poorly understood but may include systemic venous hypertension, mild CSF malabsorption (observed in PTC associated with Chiari malformations), or deleterious effects on arachnoid villi CSF reabsorption caused by toxin administration.

Modeling the dynamic relationships of the CNS, such as the pressure between the vasculature, brain parenchyma, and CSF spaces or imbalances between production and absorption of CSF,

could provide insight to the etiology of this condition (Linninger et al. 2009c). Models derived to aid in the understanding of PTC symptoms could significantly impact treatment development. However, the open questions for study within this field remain similar to those of the other clinical CSF dyscrasias: How can we improve our understanding of the etiological nuances of the syndrome?

In summary, better management strategies for diseases of intracranial dynamics should be derived from more quantitative knowledge about CSF flow. We next review the state of the art of CSF flow analysis using medical imaging to observe CSF flow in vivo (Section 4) and computer models to quantify forces, deformations, and fluid exchange (Section 5).

4. IN VIVO QUANTIFICATION OF CEREBROSPINAL FLUID DYNAMICS

Medical images open a window into the highly interconnected intracranial compartments in normal and disease states. The imaging modalities for blood and CSF flow measurements in normal and diseased states are reviewed in this section.

4.1. Acquisition of Brain and Spine Anatomy

CSF has long TE and TR values and exhibits dark signals in T1-weighted images and bright signals in T2-weighted images in MRI. T2-weighted images are widely used for clinical diagnosis of CSF-related diseases, including hydrocephalus and aqueduct stenosis (Algin & Turkbey 2012, Battal et al. 2011, Mbonane & Andronikou 2013, Ucar et al. 2015). Besides clinical diagnosis, T1-weighted images are commonly used in image segmentation for constructing models of cerebral structures, including the CSF space, gray matter, and white matter. Multiple groups have proposed automatic or semiautomatic image processing algorithms for segmentation of the CSF space (Attique et al. 2012, Fernández et al. 2011, Hsu et al. 2015, Lemieux et al. 2003). The CSF space from the head to the sacral region can be acquired by performing multiple imaging series and image post-processing techniques, such as image mosaicking (Hernández-Mier et al. 2010, Pandey & Pati 2014, Wachinger et al. 2008). CSF flow measurements require a different imaging protocol.

4.2. Cine Phase-Contrast Magnetic Resonance Imaging for Flow Measurements

Quantitative CSF flow is measured by PC MRI (Kapsalaki et al. 2012, Lee et al. 2004), which uses a velocity encoding (VENC) gradient to generate signal contrast between flowing and stationary hydrogen atoms. VENC introduces two opposite phase stimulation gradients to the hydrogen. For stationary hydrogen atoms, the net phase is zero, and therefore, the signal is cancelled. For moving hydrogen atoms, such as those in flowing blood or CSF, their positional change produces nonzero net phase, resulting in a signal. Before PC MRI data are acquired, the user must estimate the maximum velocity for optimal data acquisition. The CSF flow velocity should be equal, or slightly less than the maximum velocity set in VENC. Velocities greater than VENC produce aliasing artifacts, and velocities much smaller than VENC result in weak signals. Typically, a VENC value for standard CSF flow imaging is 5–8 cm/s (Alperin et al. 2005, Uftring et al. 2000, Wentland et al. 2010, Yoshida et al. 2009). Cardiac gating, which synchronizes MRI acquisition with the cardiac cycle, can enhance the sensitivity in pulsatile CSF measurements (Bergstrand et al. 1985, Bhadelia et al. 1995, Nitz et al. 1992). It can be performed with an electrocardiogram by two different methods: prospective gating and retrospective gating. In prospective gating, the image acquisition is triggered by the R wave via the electrocardiogram. In retrospective gating, the R wave is tracked by computer, and the data are acquired throughout the cardiac cycle. More accurate results can be obtained with retrospective gating than with prospective gating (Nitz et al. 1992).

4.3. Quantification of Blood Flow

Besides CSF flow, PC MRI is also used for blood flow measurements or quantitative magnetic resonance angiography (Brisman et al. 2012, Ducoffe et al. 2012, Prabhakaran et al. 2009), which uses time-of-flight pulse sequences and PC MRI to visualize extracranial and intracranial vascular anatomy and measure volumetric blood flow. Typically, the VENC for cerebral arteries is 60–80 cm/s (Özsarlak et al. 2004, Reimer & Boos 1999, Ross et al. 1993). In addition to velocity measurements, the volumetric flow rate can also be acquired using commercial software. NOVA from VasSol, Inc., provides volumetric flow rates, waveforms, velocity, and flow direction (Esfahani et al. 2014, Navarro et al. 2014, Zhao et al. 2007). A typical NOVA report interface is shown in **Figure 4**. Cerebral blood flow measurements have been shown to be a valuable guide for planning and outcome assessments of cerebrovascular interventions (Amin-Hanjani et al. 2007, Bauer et al. 2009, Charbel et al. 2004).

4.4. Quantification of Cerebrospinal Fluid Flow Phase-Contrast Magnetic Resonance Imaging

Compared to blood flow measurements, CSF flow measurements are less accurate because of its smaller magnitude and reversal in flow direction. CSF spaces also do not conform to the near-cylindrical shapes of cerebral blood vessels, which complicates the determination of perpendicular planes needed in volumetric flow measurements. These difficulties diminish the precision in CSF flow measurements (Stalder et al. 2008, Taviani et al. 2010, Wentland et al. 2010). Moreover, the long stretch from the head to the sacral region makes it tedious to measure CSF flow throughout the neuronal axis.

4.5. 4D Magnetic Resonance Imaging

Because of limitations of point velocity measurements by PC MRI, researchers have begun to deploy volumetric acquisition protocols with cardiac-gated PC MRI, also known as 4D MRI (Bunck et al. 2011, 2012). Two approaches are investigated in 4D MRI development: fast 3D MRI to acquire volumetric images in real time and fast 2D MRI to acquire images from all respiratory phases continuously and retrospectively sort these images. The first approach is typically accomplished with parallel imaging and echo-sharing techniques. However, current hardware and software fail to acquire high-resolution 4D image sets. The typical temporal resolution of real-time 4D MRI is greater than 1 s, and the voxel size is 4 mm (Markl et al. 2003). Overall, the image quality of real-time 4D MRI is low given the lack of spatial resolution. The loss of image quality can be partially compensated for by coregistration with high-quality reference images. The second approach requires a respiratory surrogate to monitor patient motion during image acquisition (Cai et al. 2011). Compared to real-time 4D MRI, the image quality is improved, motion artifacts are largely reduced given the fast image acquisition, and the voxel size is smaller with increased spatial resolution. Disadvantages of this technique include a longer acquisition time as every other image is acquired purely for sorting purposes.

4.6. Perspective on Current Developments and Future Directions in Cerebrospinal Fluid Flow Quantification

Current developments in CSF measurements using MRI involve imaging sequence design for faster acquisition and finer resolution. Contrast-enhanced MRI using gadolinium as a biomarker is also used for better highlighting of transport phenomena (Ragheb et al. 2014, Tumani et al. 2008, Vanopdenbosch et al. 2011). Other imaging techniques can provide additional information

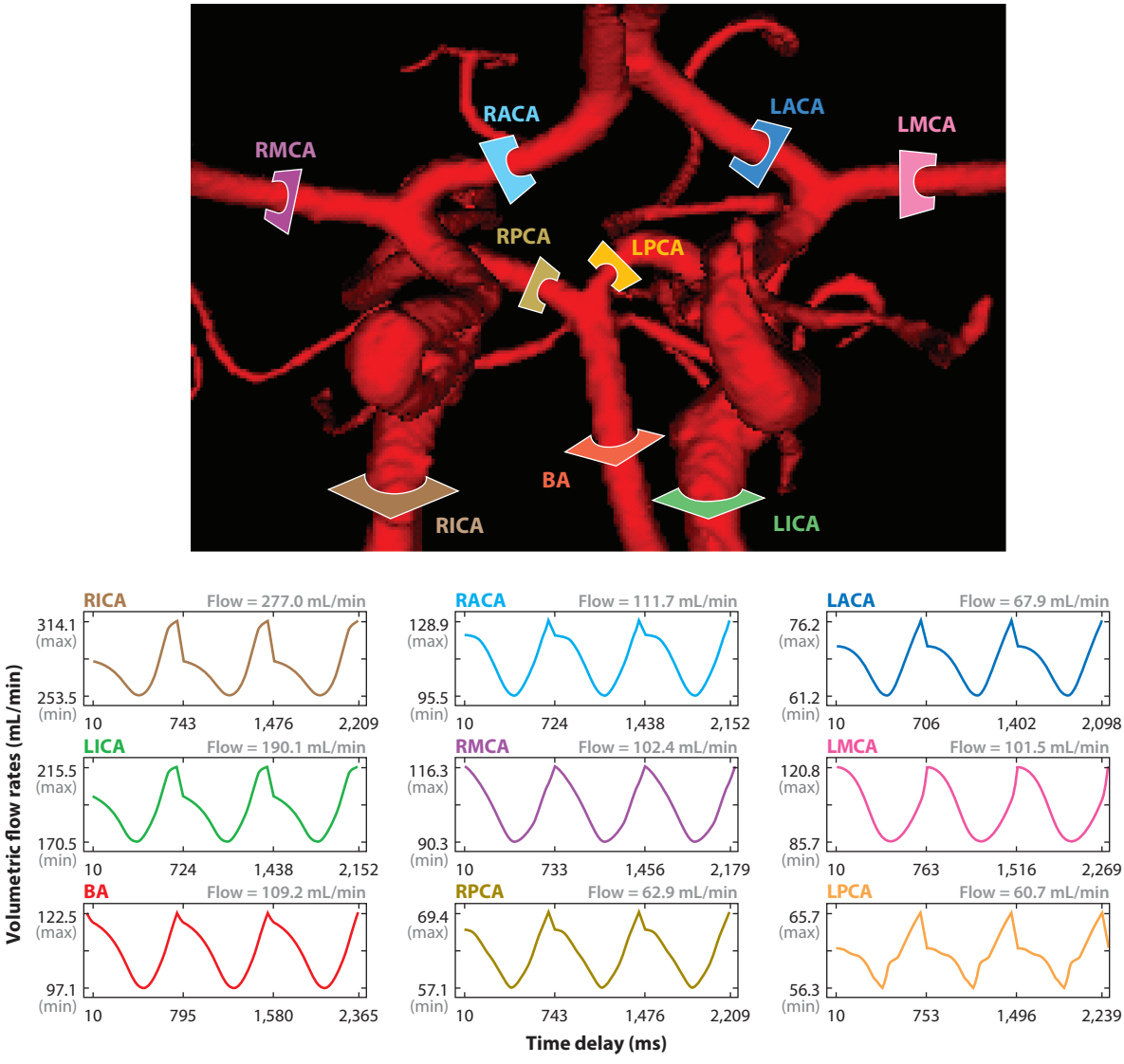

Figure 4

Cerebral blood flow measurements (NOVA, VasSol, Inc.) using time of flight for 3D acquisition of the cerebral vasculature and phase-contrast magnetic resonance angiography for blood flow measurement in major cerebral arteries (*top*). Pulsatile volumetric flow rates in the main cerebral arteries are shown on the bottom. Figure adapted from Zhao et al. (2007). Abbreviations: BA, basilar artery; LACA, left anterior cerebral artery; LICA, left internal carotid artery; LMCA, left middle cerebral artery; LPCA, left posterior cerebral artery; RACA, right anterior cerebral artery; RICA, right internal carotid artery; RMCA, right middle cerebral artery; RPCA, right posterior cerebral artery.

to monitor CSF dynamics, such as tracking radiolabeled tracer distributions using positron emission tomography. Positron emission tomography-computed tomography can facilitate the measurement of drug distribution, which is driven by CSF pulsatility following intrathecal injection (Papisov et al. 2012).

5. MATHEMATICAL MODELS OF NORMAL AND PATHOLOGICAL CEREBROSPINAL FLUID DYNAMICS

This section reviews computational models for CSF flow in the cranium, spine, and closed models for the entire CNS. The section is organized into the following subsections: intracranial models (Section 5.1), spinal flow models (Section 5.2), and models of CSF flow for the entire CNS (Section 5.3). Experimental benchtop models to validate computer predictions are discussed in Section 5.4. A brief overview of the computational model studies is provided in **Table 2**.

5.1. Compartmental Models of Intracranial Dynamics

Compartmental models pose balance equations for pulsatile volumetric deformations and compartmental pressures, fluid exchange, and bulk flows to quantify system interactions among CSF flow, blood, and nervous tissue. Momentum equations are often simplified with the Hagen-Poiseuille law of viscous fluid friction as in an idealized resistor. The fluid-structure interaction (FSI) is expressed as a pressure-dependent ideal capacitor. Viscous dissipation is often neglected or enters as velocity-dependent dampening.

The fluid and momentum exchange of intracranial dynamics was explored in a series of papers with an emphasis on the relationship between pulsatile cerebral blood flow and dynamic CSF motion (Cohen et al. 2009, Egnor et al. 2001, Sivaloganathan et al. 1998, Zagzoule & Marc-Vergnes 1986). Sorek et al. (1988a,b, 1989) introduced a cerebrovascular system with CSF, blood, and a deformable brain parenchyma. They calculated the amplitude and timing of volumetric expansion, ICPs, and volumetric fluid exchange as functions of arterial blood pressure pulsations. Stevens & Lakin (2000) incorporated the effect of interventricular fluid infusion on the ICP in Sorek et al.'s model. The spinal SAS was missing in both approaches; thus, the role of spinal compliance was not addressed.

Linninger et al. (2005) created a dynamic model of the ventricular system to test the hypothesis that choroid plexus expansion drives CSF flow in this system. Later extensions incorporated the entire CNS with full interaction of the expanding vasculature, the brain parenchyma, the ventricular system, and a compliant spine (Linninger et al. 2009c). Sample figures of three computational models are shown in **Figure 5**.

Compartmental models compute the net fluid exchange among compartments needed to set suitable boundary conditions in spatially distributed fluid dynamic (CFD) models. CFD can simulate CSF flow patterns consistent with biomechanical principles such as the Navier-Stokes equations, porous media flow, and the FSI of fluid flow within distensible boundaries.

Early CFD approaches aimed at predicting the CSF flow in short open sections of the ventricular systems. Jacobson et al. (1996) compared the flow through an hourglass-shaped cylinder, approximating the aqueduct, at steady and pulsatile conditions. They concluded that a pressure drop of only 1.1 Pa was necessary to drive CSF flow through the aqueduct. Haslam & Zamir (1998) developed analytical solutions for pulsatile flow in tubes with an elliptic cross section representing the aqueduct. Kurtcuoglu et al. (2005a,b) investigated the flow in an open model of the aqueduct and the third ventricle of normal and hydrocephalic patients initially with idealized geometries; they then repeated the computations using geometries reconstructed from anatomical models. Choroid CSF production was set, and the pressure and pulsatile pressure boundary conditions in the lateral ventricle and the foramen of Magendie were specified to achieve the desired flow rates. All tissue boundaries except for the third ventricle were assumed rigid. Linninger et al. (2005) performed a 2D simulation of the CSF flow though the lateral ventricles, aqueduct, and third and fourth ventricles. Hadzri et al. (2011) predicted CSF flow through the third ventricle and normal and stenosed aqueducts.

Table 2 Overview of CFD model approaches to CSF dynamics in the CNS

Reference	Focus of study	Microanatomy	Domain	Experimental validation
Global models of the CNS				
Tangen et al. (2015)	Studied impact of spinal microanatomy on complex flow profiles and on drug dispersion.	Trabeculae, nerve roots	3D CNS	PC MRI
Hsu et al. (2012)	Quantified effect of CSF pulsations on drug-distribution rate and spread.	Nerve roots	2D CNS	Cine MRI
Howden et al. (2011)	Examined pulsatile ventricles and rigid spinal SAS and predicted CSF peak velocity magnitude.	Trabeculae, porous	3D CNS	NA
Sweetman & Linninger (2010)	Predicted CSF flow fields in entire CNS with pulsatile boundaries.	None	3D CNS	PC MRI
Cranial models				
Buishas et al. (2014)	Predicted water transport between the compartments of the cranial vault, parenchyma, vasculature, and CSF as driven by osmotic pressure and Starling forces.	None	Compartmental model cranial SAS, cerebral vasculature, and ECS	None
Sweetman & Linninger (2011)	Compared healthy and hydrocephalic model with FSI to measured data.	None	3D cranial SAS	PC MRI
Hadzri et al. (2011)	Predicted CSF flow and pressure in normal and stenosed aqueduct.	None	Third ventricle, aqueduct	NA
Gupta et al. (2010)	Predicted velocity and pressure distributions in the cranial SAS.	Trabeculae, porous	Cranial SAS	PC MRI
Linninger et al. (2009b)	Compared healthy and hydrocephalic MRI data to simulated CSF velocity values; predicted resorption influence on ventricular enlargement.	None	Cranial SAS	PC MRI
Kurtcuoglu et al. (2007)	Made subject-specific CSF flow predictions and examined aqueduct flow jet and recirculation.	None	Third ventricle, aqueduct	MRI velocity
Linninger et al. (2007)	Predicted CSF flow patterns and pressure gradients in healthy and hydrocephalus patients for CSF spaces and porous brain parenchyma.	None	Cranial SAS, porous parenchyma	MRI velocity
Kurtcuoglu et al. (2005a)	Predicted CSF flow in simplified ventricular geometries.	None	Ventricles	MRI velocity
Linninger et al. (2005)	Quantified pulsatile CSF and approximate parenchyma deformation.	None	Ventricles	Canine ICP and human PC MRI
Haslam & Zamir (1998)	Examined pulsatile flow in elliptical cross sections.	None	Simple ellipse	NA
Jacobson et al. (1996)	Computed pressure drop in an hourglass cylinder to predict pressure drop.	None	Simple cylinder	NA

(*Continued*)

Table 2 (*Continued*)

Reference	Focus of study	Microanatomy	Domain	Experimental validation
Spinal models				
Pahlavian et al. (2014)	Assessed impact of nerve roots and denticulate ligaments on CSF flow patterns.	Nerve roots, denticulate ligaments	Cervical	4D PC MRI
Cheng et al. (2014)	Predicted effect of FSI of spinal cord on fluid flow.	None	Cervical	PC MRI
Yiallourou et al. (2012)	Compared 4D MRI flow profiles with subject-specific CFD.	None	Cervical	4D PC MRI
Rutkowska et al. (2012)	Assessed cyclic CSF flow in Chiari patients before and after decompression surgery.	None	Cervical	PC MRI
Gupta et al. (2009)	Predicted pressure and flow profiles for full cardiac cycle and observed no net flow.	Trabeculae, porous	Craniocervical	MRI velocity
Roldan et al. (2009)	Compared flow profiles in Chiari patient and healthy subject.	None	Cervical	2D PC MRI
Linge et al. (2010)	Predicted spatial CSF velocities for the full cardiac cycle.	None	Craniocervical	PC MRI
Stockman (2007)	Studied impact of microanatomy on flow patterns with lattice Boltzmann simulations.	Trabeculae, nerve roots	Annular model of spine	MRI-derived flow profile
Loth et al. (2000)	Studied flow in short segments of the spine and impact of annular geometric variation.	None	Axial segments	MRI peak velocity

Domains are subject specific, unless otherwise noted. Abbreviations: CFD, computational fluid dynamics; CNS, central nervous system; CSF, cerebrospinal fluid; ECS, extracellular space; FSI, fluid-structure interaction; ICP, intracranial pressure; MRI, magnetic resonance imaging; NA, not available; PC MRI, phase-contrast magnetic resonance imaging; SAS, subarachnoid spaces.

In FSI models, deformable boundaries aim to incorporate vascular coupling between blood and CSF flow. CSF flow simulations were performed in an open ventricular system and incorporated brain motion by specifying the explicit boundary grid motion of each node belonging to the third ventricle and aqueduct (Kurtcuoglu et al. 2007). Linninger et al. (2007) presented a closed model of the CNS with FSI in which the timing of the expanding vasculature was gated with blood flow measured in the basilar artery. The volumetric strain of the vascular expansion was transmitted through a deformable parenchyma to the ventricular system, with the moving walls of the choroid plexus and periventricular areas setting in motion pulsatile CSF flow. Comparison with magnetic resonance measurements showed that the proposed FSI model was able to predict global flow patterns equally well as those currently available from medical imaging. The model also predicted ICF diffusion through the ECS of the poroelastic parenchyma. Sweetman et al. (2011) presented a 3D FSI model for CSF in the ventricular system and the cranial SAS with subject-specific geometry for hydrocephalic and healthy subjects. The predictions compared well to MRI velocity measurements.

5.2. Cerebrospinal Fluid Flow Models in the Spine

Earlier models of CSF flow in the spine concerned small sections of the CNS with idealized geometries. Loth et al. (2000) studied the CSF flow for separate short segments along the spine. By adjusting the boundary conditions for each segment, the authors solved the equations of

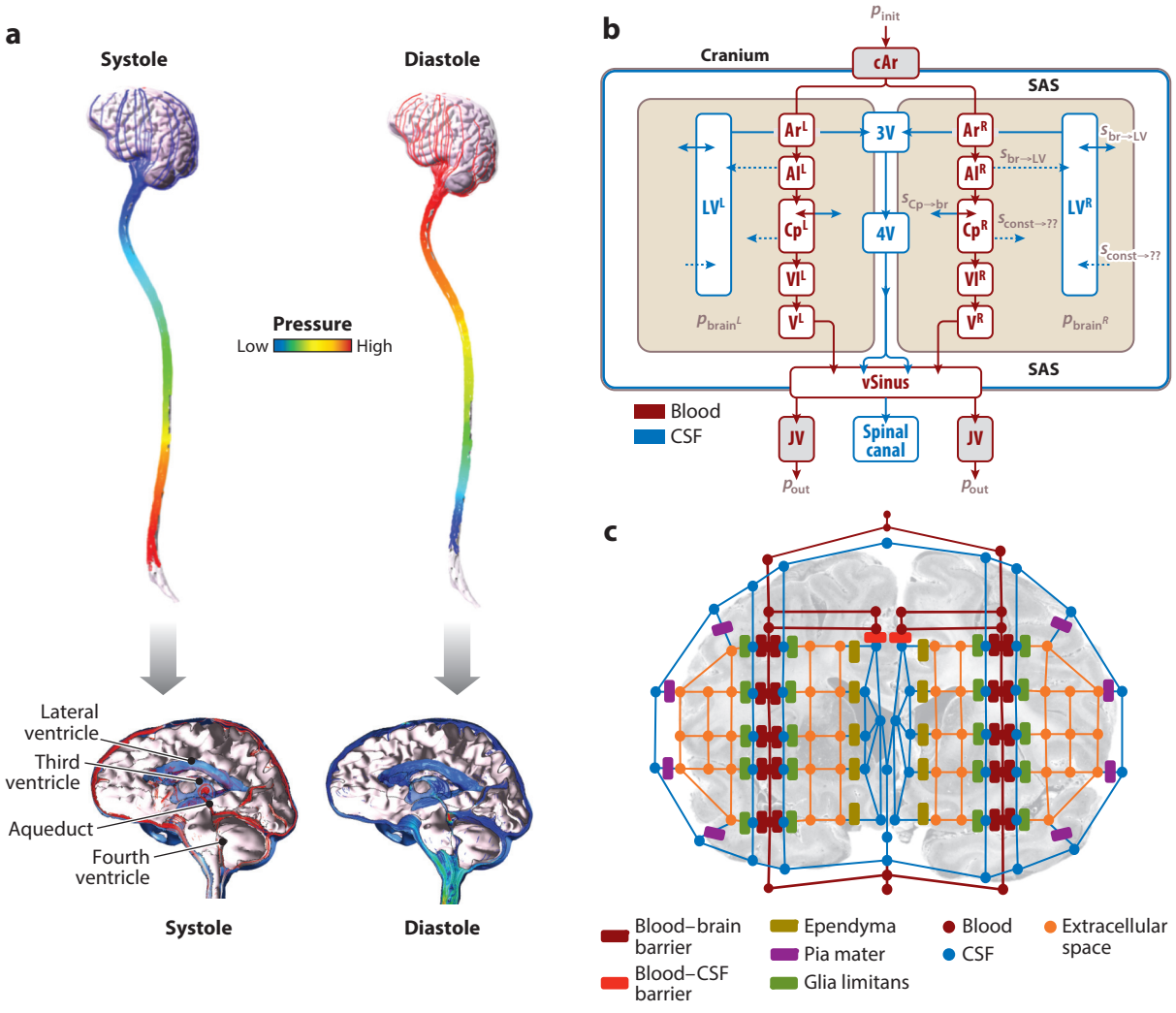

Figure 5

The computational domain of three computational models of intracranial dynamics. (*a*) 3D subject-specific simulation of CSF flow dynamics in the full cranial and spinal SAS are shown with pressure streamlines at peak systole and peak diastole. Additionally, a magnified view of the cranial vault and ventricles shows the pressure distribution in LV, 3V, 4V, Aq, and prepontine area during peak systole and diastole. Panel *a* adapted from Tangen et al. (2015). (*b*) A compartmental model of central nervous system dynamics comprising three main components: the ventricular system, the cerebral and spinal SAS, and the parenchyma. Panel *b* taken with permission from Linninger et al. (2009c). (*c*) A network model for water transport in the cranial vault between blood-tissue, tissue-CSF, and CSF-blood. The model examines the effect of osmolarity and Starling forces on fluid flow between compartments of the central nervous system. Panel *c* adapted from Buishas et al. (2014). Abbreviations: 3V, third ventricle; 4V, fourth ventricle; Al, arterioles; Aq, aqueduct; Ar, arteries; BBB, blood-brain barrier; cAr, cerebral artery; Cp, capillaries; CSF, cerebrospinal fluid; ECS, extracellular space; JV, jugular vein; LV, lateral ventricle; SAS, subarachnoid spaces; V, veins; VI, venules; vSinus, venous sinus.

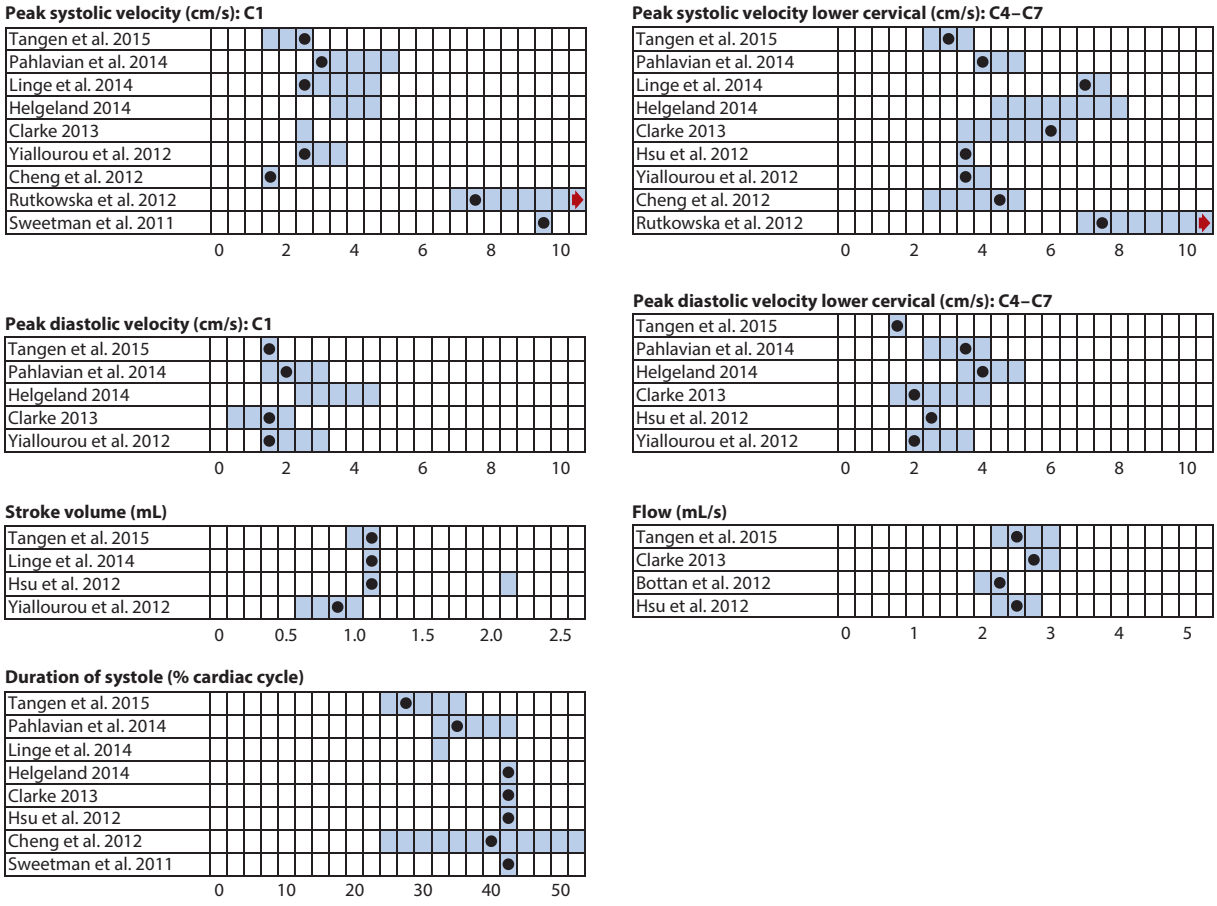

Figure 6

Summary of cerebrospinal fluid flow parameters in the human spine predicted by computational fluid dynamic models. Blue boxes represent the data range, and black points represent the average value; red arrows indicate data values that extend beyond range.

CSF motion in 1-cm-long sections of the spinal SAS and compared the computed fields inside the annular shapes to flow measurements. A comparative list of CSF flow measurements and predictions in the spine found in the open literature is presented in **Figure 6**. Gupta et al. (2008) derived analytical solutions of the fluid flow and pressure drop for a straight elliptical annulus. Linge et al. (2010) solved 3D CSF flow in the craniovertebral junction and cervical spine to predict spatial CSF velocities in each cardiac cycle.

Other approaches used medical image reconstruction to represent subject-specific anatomical spaces to enhance model fidelity. **Supplemental Table 1** gives a summary of software tools for image reconstruction and CFD simulations (follow the **Supplemental Material link** from the Annual Reviews home page at **http://www.annualreviews.org**). Roldan et al. (2009) reconstructed cervical spinal SAS segments for healthy subjects and Chiari patients and found high-velocity jets in the Chiari subjects. Rutkowska et al. (2012) simulated CSF flow velocities for an open cervical spine segment for healthy subjects and Chiari patients. They determined that peak CSF velocities, pressure gradients, and the duration of bidirectional flow increase in the pathological state.

Supplemental Material

Cheng et al. (2014) reconstructed a patient-specific model for an open section of cervical and thoracic SAS. The dural surface was assumed rigid; the pial surface models were deformed by exchanging the displacement at each time step between the fluid solver and the solid spinal cord (see **Figure 1** for anatomical features). The authors concluded that the pial deformations had a negligible impact on the CSF velocity and pressure profiles.

Yiallourou et al. (2012) also compared 4D MRI flow measurements in a normal subject and patients suffering from CM1 with a CFD model of an open, rigid cervical spine segment. They achieved a poor match between their CFD predictions and measured 4D MRI data and attributed this shortcoming to the lack of microanatomical features in their model.

The spinal SAS contains microanatomical aspects, including nerve roots, ligaments, and trabeculae. These aspects interfere with the CSF flow in the SAS. It is known that microanatomical aspects in the spinal canal may substantially affect CSF patterns, yet their actual impact on flow resistance has not been quantified. Haller & Low (1971) also showed that the spinal microanatomy induces complex mixing eddies. Because the length scale of microanatomical aspects is below medical image resolution, computational analysis is a useful tool to assess their effects of microfluid patterns and flow resistance.

Based on the same data as used by Yiallourou et al. (2012), Pahlavian et al. (2014) studied the influence of nerve roots on CSF flow by adding artificial nerve pairs to a section of the cervical spine modeled as a open, rigid annular space. The CFD simulation results indicated that nerve roots increased peak velocities and prolonged the duration of bidirectional flow.

Stockman (2005, 2007) studied the impact of nerve roots and trabeculae on convective flow with lattice Boltzmann simulations in idealized cylindrical spine models. He concluded that regularly spaced trabeculae had a limited impact on global flow patterns; however, he noted that his study did not address complex trabeculae formations as they occur in the spinal anatomy. Gupta et al. (2009) also studied the effect of microanatomical aspects on flow resistance computationally. Based on a simulated porous model of the cerebellomedullary cistern and the spinal SAS, they concluded that the subresolution microstructure density and radius can triple the pressure drop in CSF flow. The authors proposed the addition of an anisotropic friction term to the fluid flow equations. The porous-medium adaptation then increased the flow resistance as expected.

Recently, Tangen et al. (2015) presented a novel computational meshing approach to quantify the contribution of microanatomical aspects on CSF flow patterns and flow resistance within the entire CNS. Cranial and spinal CSF-filled compartments were reconstructed from human imaging data, including nerve roots up to the limit of imaging resolution; microscopic trabeculae below the image-detection threshold were added artificially. CSF pulsations were enforced through the deformation of the parenchyma and lateral ventricle. Spinal compliance was incorporated by explicit boundary deformations. The timing and extent of the spinal deformations for the cervical to the sacral regions were inferred from the phase lag and attenuation of the velocity peak amplitude of CSF velocity fields acquired with cine MRI in a volunteer. Volumetric flow profiles were matched at three spinal levels with measured MRI values. The CSF flow fields and the microcirculatory-induced flow patterns were computed using massive parallelization on the Blacklight supercomputer.

A significant outcome of Tangen et al.'s (2015) study was the demonstration that microanatomical aspects generate geometry-induced flow patterns. **Figure 7** shows the microanatomy-induced fluid patterns in a C4–C6 section of the spinal SAS. The unique properties of geometry-induced flow patterns have been described previously in engineering systems (Mackley & Ni 1991, Piot & Tavoularis 2011). Nerve roots also generate complex vortices, but more importantly, spinal trabeculae were found to induce regions of microcirculation, with their location, size, and vorticity along the spine characterized. Tangen et al.'s (2015) CFD study also suggested a 2–2.5-fold increase in

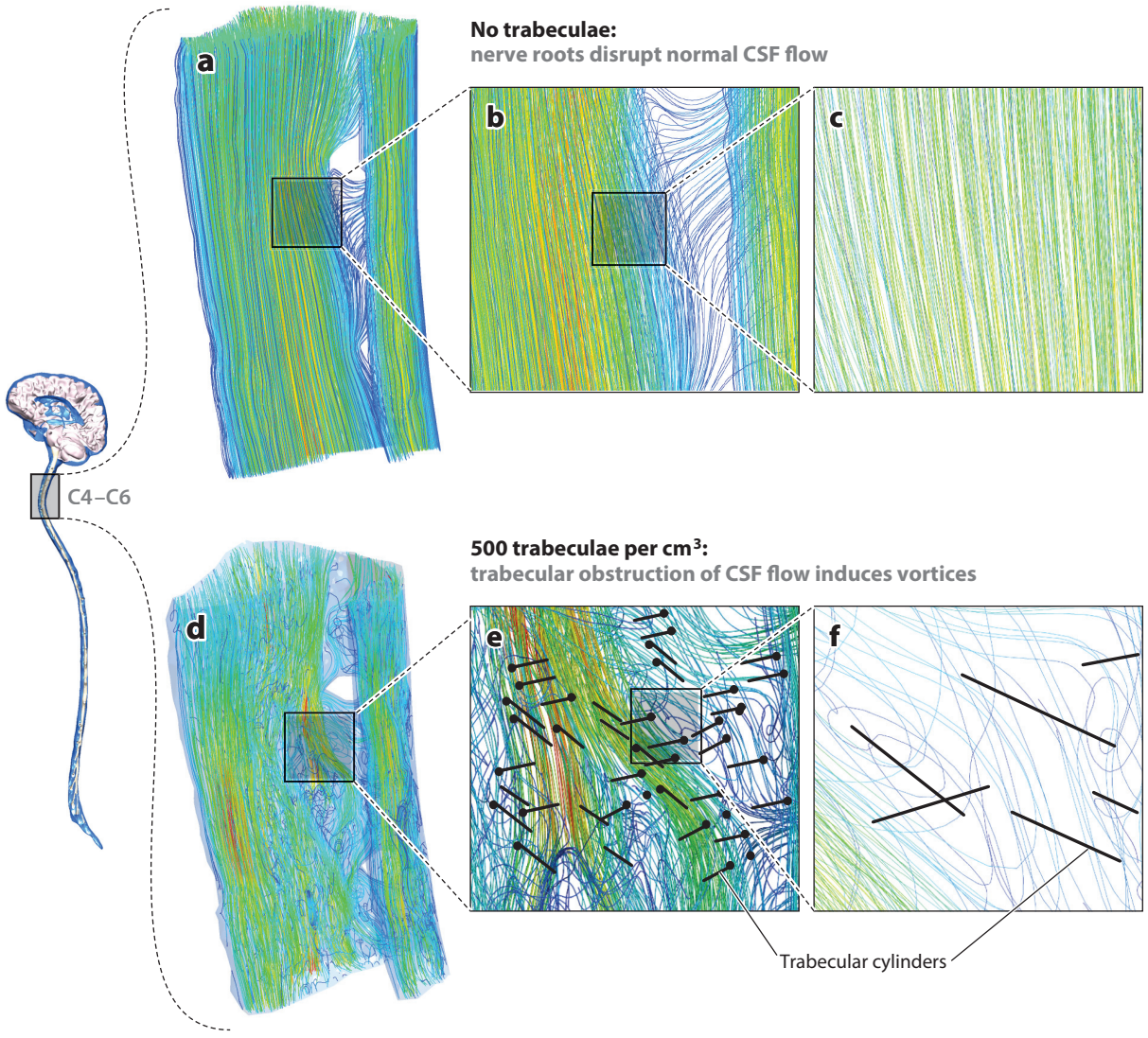

Figure 7

Rigorous computation fluid dynamics simulations showing the effect of microanatomical features on cerebrospinal fluid (CSF) flow patterns in the spine. (*a–c*) Results in a 5-cm-long segment at the C4–C6 cervical region with nerve roots but no trabeculae. Velocity streamlines reveal that nerve roots disrupt the otherwise laminar CSF flow profiles and introduce regions of circular flow in the vicinity of the nerves. (*d–f*) Simulation results in the same cervical spine segment with about 500 trabeculae per centimeter. Here, the fluid domain is obstructed by thin trabeculae cylinders (*black streaks in e and f*). This model requires a massive mesh of 54 million elements to resolve the flow field around microscopic trabeculae and nerve roots. The induction of vortices around trabeculae is shown with increasing magnification in panels *e* and *f*. Figure adapted from Tangen et al. (2015).

the pressure drop mainly owing to arachnoid trabeculae. Microanatomy-induced fluid patterns coupled with the asymmetric CSF pulsatile waveform were found to be responsible for the rapid caudocranial spread of an intrathecally administered drug. The speed of rostral drug dispersion is drastically accelerated through pulsatile flow around microanatomy-induced vortices.

5.3. Models of Cerebrospinal Fluid Flow in the Entire Central Nervous System

Most existing CFD models use rigid walls and open cross sections delineating only a specific subdomain of the CSF-filled spaces, such as a short segment of the SAS. In open rigid wall models, CSF is allowed to exit the computational domain, and boundary conditions are adjusted so that the desired or measured velocities can be achieved. In vivo CSF flow does not occur in a rigid system with open boundaries. This limitation of CFD models has been pointed out in a recent review (Kurtcuoglu 2011).

Less work has been conducted on closed models of the CSF flow in the entire CNS. Closed models do not have open adjustable boundary conditions but need to account for the CSF displacement by proper force coupling with the distensible vasculature or compliant boundaries. A full CNS model of CSF flow with deformable walls was developed by Linninger's group (Linninger et al. 2009c, Penn et al. 2011, Sweetman & Linninger 2010, Sweetman et al. 2011). A major contribution of this model was the prediction of CSF velocities through the entire CNS as driven by the cerebrovascular pulsations, as well as realistic phase lags between the arterial and venous blood vessels, CSF motion in the ventricles with oscillatory CSF displacement between cranial and spinal SAS, and the deformation of the spinal SAS. Also, it was found that CSF velocities peak in the cervical spine and decrease caudally. Howden et al. (2011) performed simulations on the full CNS with deformable ventricles but with rigid spinal SAS. The impact of microanatomical flow resistance was accounted for by porous medium friction. Their model predicted the spinal CSF velocities to be very small. To improve the predictions, the authors suggested that spinal wall motion should be included possibly as a function of inspiration. The model of CSF flow proposed by Linninger's group has recently been extended to a subject-specific 3D model with explicit fluid interaction of the CSF and the spinal compartment (Tangen et al. 2015). To date, this CFD model is the first to quantify CSF in the entire CNS with the inclusion of microanatomy-induced mixing patterns.

Beyond their significance in describing abnormal flow in CNS diseases, flow simulations are important for predicting the biodistribution of drugs released into the CSF. Stockman (2007) computed the drug spread within an elliptical spine model containing nerve roots and regular trabeculae arrangements and found a 5- to 10-fold increase in solute dispersion. There is a growing interest in the pharmaceutical industry in determining the biodistribution of drugs in the CSF. For example, Novartis conducted a study in which CFD simulations were performed to predict the drug distribution after intrathecal injection. Results by Kuttler et al. (2010) are shown in **Figure 8*a***. Additionally, the authors found that the injection orientation had a local impact and postulated that injection parameters could influence the global drug spread. The pulsatility and frequency of spinal CSF flows were identified as key factors for the speed and spatial distribution of intrathecally administered drugs (Hsu et al. 2012). Tangen et al. (2015) also conducted drug-distribution simulations and found that microanatomy-induced fluid patterns were responsible for the rapid caudocranial spread of intrathecally administered drugs (**Figure 8*b***). These predictions were validated with in vitro 3D experiments of the human spine. These findings are highly significant, as intrathecal drug administration is receiving attention as a route for the effective delivery of gene and enzyme replacement therapies bypassing the blood-brain barrier (Calias et al. 2012, 2014; Papisov et al. 2012, 2013). Closed models of the CSF flow in the entire CNS are becoming an ideal in silico test bed for pharmacokinetic studies of intrathecally administered drugs or gene therapies.

5.4. In Vitro Studies of Cerebrospinal Fluid Flow

Owing to the inaccessibility of flow and pressure fields, CSF flow phenomena were studied by several groups with in vitro experimental benchtop systems. A very realistic geometrical model of the cranial SAS and ventricular system is shown in **Supplemental Figure 1** (Bottan et al.

Supplemental Material

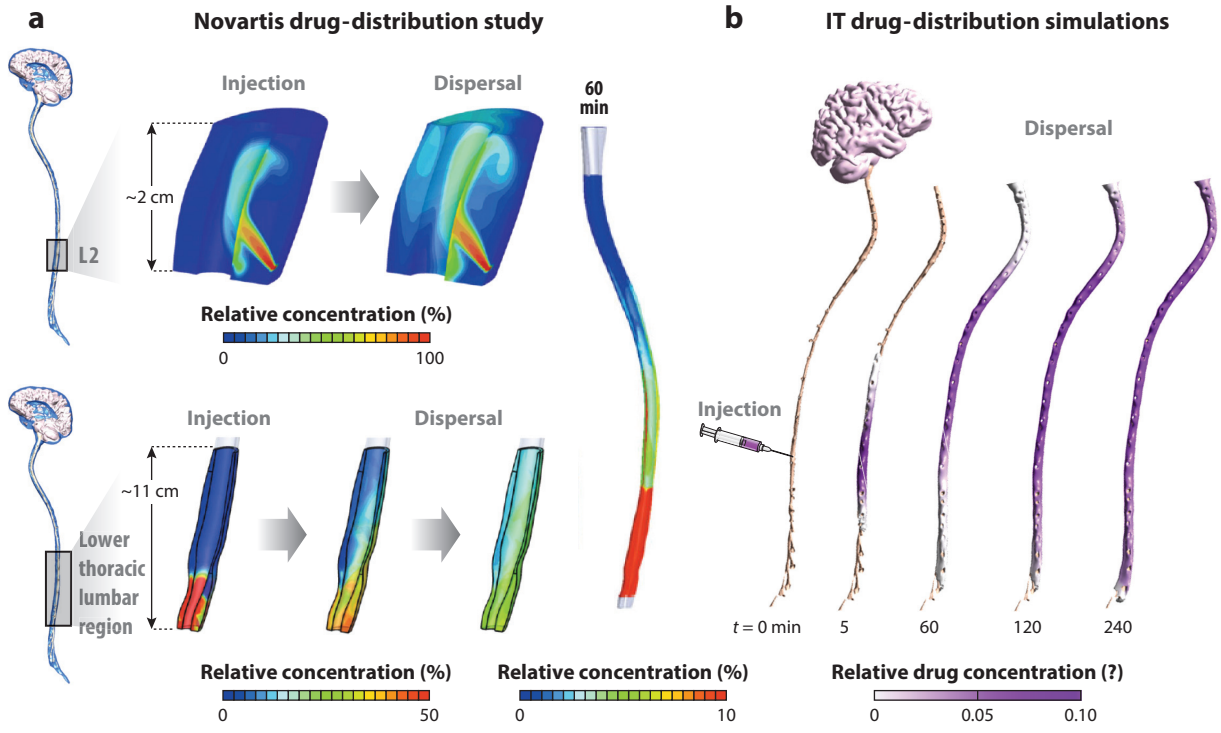

Figure 8

Simulated drug distribution after lumbar injection into the central nervous system. (*a*) The drug profile during injection and dispersion in an open model of the spinal subarachnoid spaces (SAS) in a study conducted by Novartis to predict drug distribution. Panel *a* adapted from Kuttler et al. (2010). (*b*) Simulated intrathecal (IT) drug distribution in a complete closed 3D model of the cranial and spinal SAS based on Tangen et al. (2015). The drug front rapidly ascends toward the brain.

2012, 2013). Martin and colleagues fabricated annular models of the spinal SAS with stenosis or Chiari malformations to observe pressure changes in the system (Martin & Loth 2009, Martin et al. 2010). In addition, the effect of coughing on the spinal CSF pressure was simulated. Spinal CSF flow patterns due to microanatomical aspects were also studied in an in vitro spine model with deformable boundaries (Hettiarachchi et al. 2011). In experimental tracer distribution studies, microanatomy-induced vortices were found to substantially enhance drug transport in an intrathecally injected drug (Hsu et al. 2012).

6. DISCUSSION

This section summarizes the state of quantitative knowledge about cranial and spinal CSF flow. We assess current research in Section 6.1, followed by a discussion of the relevance of computer modeling for better clinical management of diseases of intracranial dynamics in Section 6.2. Section 6.3 highlights clinical applications of CFD.

6.1. Computational Fluid Dynamics

As demonstrated by the recent increase in relevant publications, iCFD techniques for the study of intracranial dynamics in normal and disease states are becoming widely established in research

labs. There has also been growing attention given to CSF dynamics in the pharmaceutical industry (e.g., Kuttler et al. 2010).

Detailed computational models are a useful tool to resolve flow and pressure fields, beyond the scope of imaging modalities, in space and time. They are valuable to elucidate small changes in CSF flow patterns in diseases (e.g., CM1). In iCFD, computational domains are reconstructed with image segmentation software; many useful tools are listed in **Supplemental Table 1**. The use of computational meshes with subject-specific geometry enables the direct comparison of simulations with in vivo data acquired for an individual subject. The lack of anatomical features, uncertainty in the boundary assignments, and omission of FSIs contribute to the observed discrepancies between detailed CFD predictions and patient-specific flow measurements.

Supplemental Material

Better image quality and measurements are expected to narrow the gap between computer predictions and imaging data. Areas in need of more work include the precise incorporation of microanatomical features in the SAS, the automatic reconstruction of the subject-specific cerebrovascular tree, and the representation of the deep cortical gyri. Advances in imaging (e.g., 4D MRI) are expected to provide volumetric flow data in real time, which will be an improvement over point velocity measurements using multiple heartbeat averages.

Integrated mathematical models enforce assumptions about the mass and momentum exchange in the entire CNS. Integrated models are well suited for hypothesis testing because only a few external boundary conditions, such as the arterial pulse waveforms, are needed. Existing knowledge gaps about the ICP and deformations will have to be addressed in integrated models before detailed simulations can be safely formulated. Only recently has research begun to construct 3D subject-specific integrated models with FSI to predict velocities, ICPs, and volumetric deformations for the entire CNS.

6.2. Future Directions of Central Nervous System Models

This section outlines a road map for future, more holistic brain models of intracranial dynamics. Three areas are expected to garner future research in biomechanics and biofluidics.

6.2.1. Automatic segmentation of the cerebrovascular tree. Next steps to address the coupling of cerebral blood flow and CSF dynamics are expected from improved cerebrovascular tree representations, coupled with blood vessel wall mechanics, tissue deformation, and CSF displacements. A subject-specific vascular tree reconstructed from medical images is shown in **Figure 2**. Multidomain CFD will entail a distensible arterial tree submersed in pulsatile brain fluids. Global and microcirculatory cerebral blood flow patterns (Gould & Linninger 2015, Linninger et al. 2013) will be made computationally tractable using multiscale model-reduction techniques (Huyghe et al. 1988, 1989; Hyde et al. 2013). Structured parametric meshes promise drastic mesh-size reductions, while simultaneously improving computational performance and accuracy (Ghaffari et al. 2015). Organ-wide cerebral blood flow simulations coupled with CSF flow will become tractable with massively parallel computer clusters (Towns et al. 2014).

6.2.2. Fluid-structure interaction with Euler-Lagrangian mesh deformations. FSI techniques with deformable moving computational meshes, as described by Shyy et al. (2012), will be deployed to determine the timing and extent of deformations occurring between the vasculature and the CSF as well as spinal deformations. In vivo measurements of the gradual increase in the phase lag and the diminishing amplitude of the spinal velocity fields observed in the caudal direction of the neuronal axis will help characterize the spatial distribution of the spinal compliance.

6.2.3. Mass exchange linking the vascular to the interstitial and cerebrospinal fluid compartments. Brain deformation under short time load (Johnston et al. 2004, Zakharov et al. 2003) will be characterized using poroelastic (Tully & Ventikos 2009) or mixing theories (Ehlers & Wagner 2013, 2015; Wagner & Ehlers 2010, 2012). A first attempt to compute fluid exchange and size changes of the ECS due to osmolar pressure gradients has been presented by Buishas et al. (2014).

6.3. Clinical Applications

Apart for the fundamental knowledge gain, which clinical aspects are expected to be impacted by future computational models of CSF dynamics? Among several novel developments of clinical applications (Armonda et al. 1994, Cheng et al. 2012, Sundström et al. 2010, Yang et al. 2013), three specific applications highlight the potentially high impact computations will have on clinical practice.

6.3.1. Computer-aided design of biomedical devices. The design and optimization of ventricular shunts have been conducted with the help of CFD tools (Galarza et al. 2013, 2014). Moreover, fluid mechanical design and operation of implantable components are often performed in silico to optimally prepare prototypes for animal testing. Examples include the positional dependence of catheter placement (Linninger et al. 2009a), optimal design of catheter ports (Galarza et al. 2015), and prediction of convection-enhanced drug delivery (Linninger et al. 2008, Sindhwani et al. 2011).

6.3.2. Drug delivery studies in silico (gene therapy). Intrathecal drug delivery is a method to bypass the blood-brain barrier and has commonly been used for the management of spasticity (Detrembleur & Plaghki 2000, Dykstra et al. 2007, Gracies et al. 1997, Pohl et al. 2003, Van Schaeybroeck et al. 2000) or chronic pain (Bolash et al. 2015, Bruel et al. 2013, Prager et al. 2014, Raphael et al. 2013). The enormous potential of intrathecal delivery for effective administration of gene therapies to target regions in the brain or spine has been explored in primate and human trials (Calias et al. 2012, 2014; Papisov et al. 2013). The pulsation amplitude and frequency have been identified as key factors for drug dispersion after intrathecal delivery (Hsu et al. 2012, Tangen et al. 2015). Moreover, injection impulse and drug-binding kinetics influence the extent and speed of biodistribution (Bernards 2000, Bernards et al. 2003, Yaksh & Noueihed 1985, Yaksh et al. 2002). Recent computer models have been shown to be in excellent agreement with experiments conducted in in vitro spinal models emulating the physical transport phenomena in humans. The experimental models used in combination with detailed 3D CFD computations of CSF motion and species transport are expected to improve the analysis of animal data and can aid in planning clinical trials, especially in pharmaceutical industry applications.

6.3.3. Prediction of transport phenomena from medical images. Invasive drug delivery can be used to circumvent the blood-brain barrier and achieve high doses in the target tissue without widespread systemic distribution. For example, brain tumors can be treated locally by inserting a catheter close to its core and releasing a chemotherapeutic agent into the adjacent brain tissue (convection-enhanced drug delivery). The temporal and spatial distribution of drugs delivered via convection enhancement or intrathecal administration is a function of transport phenomena and biochemical reaction kinetics. However, the reaction or transport rates of new therapeutic agents are unknown but can be inferred from medical images. A mathematical framework to estimate unknown reaction rate constants, tissue permeability, and molecular diffusivity for new therapeutic agents from spatially distributed medical image data has been demonstrated by Somayaji et al. (2008).

7. CONCLUSIONS

The study of intracranial dynamics with spatially distributed patient-specific computational domains poses demands that lie outside the scope of classical CFD. These areas include (*a*) FSI between blood and CSF-embedded deformable, often porous structures, (*b*) flow coupled with microcirculatory mass exchange driven by hydrostatic and osmolar driving forces, and (*c*) chemical reactions.

Spatially distributed computer predictions produce velocity, pressure, or concentration fields that can be compared with in vivo imaging results. The computer simulations have higher spatial and temporal resolution than is accessible by in vivo measurements. Predictions extend to quantities such as pressures or chemical species that are hard or impossible to measure. Computer predictions are ideal to explore the parametric sensitivity with much finer quantitative resolution than is possible experimentally.

Significant differences exist between boundary conditions in classical CFD and those in iCFD. In classical CFD, computational domains often coincide with machined object boundaries, such as turbine blades or the body of Formula One cars. In biological systems, system boundaries often do not conform to well-defined physical surfaces or cut right through the system of study. Examples include the deep gyrations of the human cortex, pial arteries traversing the cranial SAS, or the leptomeningeal layers and microanatomical features of the spinal canal. Despite these limitations, there is no alternative to iCFD for parametric studies calculating the impact of different boundary choices on the distributed system performance. It is the method of choice to test the consistency of assumptions or to create predictions that can be validated experimentally. Indeed, as many microscopic phenomena are not accessible experimentally, multiscale mathematical models are essential for analyzing and quantifying FSI and chemical reaction phenomena occurring in the CNS.

Beyond reproducing known experimental outcomes, there is the opportunity for testing new assumptions. When iCFD is used as an exploratory instrument, hard predictions are generated that quantify the functional interactions of CNS mechanics. The role of iCFD is therefore highly significant for refining the quantitative knowledge about disease progression and optimization of therapies. The outcome assessment of surgical intervention in syringomyelia is an excellent example of the emerging integration of iCFD in clinical practice (Rutkowska et al. 2012). iCFD was used to disarm the myth that large transmantle pressure differences cause ventricular enlargement. Later experiments in dogs confirmed the computer predictions of negligible pressure differences (Linninger et al. 2005).

It is expected that mathematical modeling validated with imaging data and in vitro experiments will gain importance as a discovery and exploration tool. Medical images, interpreted with quantitative models, will help close the knowledge gap pertaining to normal CSF dynamics and diseases of abnormal CSF dynamics.

FUTURE ISSUES

1. The arterial origin of the CSF pulsations has been established. However, mathematical modeling of cerebral blood-CSF coupling is elusive, mainly because of the size and complexity of the angioarchitecture. Recent studies suggest that the inspiration rhythm also alters the amplitude of the CSF flow signal in the aqueduct (Dreha-Kulaczewski et al. 2015).

2. How is the ICP affected by osmolarity differences? What role do osmotic pressure gradients play in normal states and pathologies, including edema and hydrocephalus? This question also challenges whether CSF production and reabsorption occur throughout the brain.
3. What are the spatial distribution and biomechanical origin of CNS compliance? Currently, detailed measurements localizing volumetric strains in the parenchyma or lumen changes affecting the vascular bed are still lacking.
4. The role of perivascular transport or fluid exchange along lymphatic pathways, as well as microflow patterns in the ECS, awaits experimental determination and computational modeling.

DISCLOSURE STATEMENT

The authors are not aware of any biases that might be perceived as affecting the objectivity of this review.

ACKNOWLEDGMENTS

The authors acknowledge partial support from an NSF EAGER grant 1340451, NSF CBET grant 1403409, and NIH grant 5R21NS071144-02. The authors thank Ms. Mahsa Ghaffari and Mr. Ben Schneller for their contributions to the reconstruction and rigorous CFD simulation of the whole arterial tree.

LITERATURE CITED

Algin O, Turkbey B. 2012. Evaluation of aqueductal stenosis by 3D sampling perfection with application-optimized contrasts using different flip angle evolutions sequence: preliminary results with 3T MR imaging. *Am. J. Neuroradiol.* 33:740–46

Alperin N, Hushek SG, Lee SH, Sivaramakrishnan A, Lichtor T. 2005. MRI study of cerebral blood flow and CSF flow dynamics in an upright posture: the effect of posture on the intracranial compliance and pressure. In *Intracranial Pressure and Brain Monitoring XII*, ed. WS Poon, MTV Chan, KYC Goh, JMK Lam, SCP Ng, et al., pp. 177–81. New York: Springer

Ambarki K, Lindqvist T, Wåhlin A, Petterson E, Warntjes MJB, et al. 2012. Evaluation of automatic measurement of the intracranial volume based on quantitative MR imaging. *Am. J. Neuroradiol.* 33:1951–56

Amin-Hanjani S, Shin JH, Zhao M, Du X, Charbel FT. 2007. Evaluation of extracranial–intracranial bypass using quantitative magnetic resonance angiography. *J. Neurosurg.* 106:291–98

Armonda RA, Citrin CM, Foley KT, Ellenbogen RG. 1994. Quantitative cine-mode magnetic resonance imaging of Chiari I malformations: an analysis of cerebrospinal fluid dynamics. *Neurosurgery* 35:214–23; discussion 223–24

Attique M, Gilanie G, Hafeez-Ullah, Mehmood MS, Naweed MS, et al. 2012. Colorization and automated segmentation of human T2 MR brain images for characterization of soft tissues. *PLOS ONE* 7:e33616

Aubin ML, Vignaud J, Jardin C, Bar D. 1981. Computed tomography in 75 clinical cases of syringomyelia. *Am. J. Neuroradiol.* 2:199–204

Auer LM, Ishiyama N. 1986. Cerebrovascular response to elevated intracranial pressure. In *Intracranial Pressure VI*, ed. PJD Miller, PGM Teasdale, PJO Rowan, PSL Galbraith, PAD Mendelow, pp. 399–403. New York: Springer

Balédent O, Gondry-Jouet C, Meyer M-E, De Marco G, Le Gars D, et al. 2004. Relationship between cerebrospinal fluid and blood dynamics in healthy volunteers and patients with communicating hydrocephalus. *Invest. Radiol.* 39:45–55

Battal B, Kocaoglu M, Bulakbasi N, Husmen G, Tuba Sanal H, Tayfun C. 2011. Cerebrospinal fluid flow imaging by using phase-contrast MR technique. *Br. J. Radiol.* 84:758–65

Bauer AM, Amin-Hanjani S, Alaraj A, Charbel FT. 2009. Quantitative magnetic resonance angiography in the evaluation of the subclavian steal syndrome: report of 5 patients. *J. Neuroimaging* 19:250–52

Bergstrand G, Bergström M, Nordell B, Ståhlberg F, Ericsson A, et al. 1985. Cardiac gated MR imaging of cerebrospinal fluid flow. *J. Comput. Assist. Tomogr.* 9:1003–6

Bering EA. 1952. Water exchange of central nervous system and cerebrospinal fluid. *J. Neurosurg.* 9:275–87

Bernards CM. 2000. Rostral spread of epidural morphine: the expected and the unexpected. *Anesthesiology* 92:299–301

Bernards CM, Shen DD, Sterling ES, Adkins JE, Risler L, et al. 2003. Epidural, cerebrospinal fluid, and plasma pharmacokinetics of epidural opioids (part 1): differences among opioids. *Anesthesiology* 99:455–65

Bhadelia RA, Bogdan AR, Wolpert SM. 1995. Analysis of cerebrospinal fluid flow waveforms with gated phase-contrast MR velocity measurements. *Am. J. Neuroradiol.* 16:389–400

Bhadelia RA, Madan N, Zhao Y, Wagshul ME, Heilman C, et al. 2013. Physiology-based MR imaging assessment of CSF flow at the foramen magnum with a valsalva maneuver. *Am. J. Neuroradiol.* 34:1857–62

Bilston LE, Fletcher DF, Brodbelt AR, Stoodley MA. 2003. Arterial pulsation-driven cerebrospinal fluid flow in the perivascular space: a computational model. *Comput. Methods Biomech. Biomed. Eng.* 6:235–41

Bilston LE, Stoodley MA, Fletcher DF. 2009. The influence of the relative timing of arterial and subarachnoid space pulse waves on spinal perivascular cerebrospinal fluid flow as a possible factor in syrinx development. *J. Neurosurg.* 112:808–13

Bolash R, Udeh B, Saweris Y, Guirguis M, Dalton JE, et al. 2015. Longevity and cost of implantable intrathecal drug delivery systems for chronic pain management: a retrospective analysis of 365 patients. *Neuromodul. Technol. Neural Interface* 18:150–56

Bottan S, Poulikakos D, Kurtcuoglu V. 2012. Phantom model of physiologic intracranial pressure and cerebrospinal fluid dynamics. *IEEE Trans. Biomed. Eng.* 59:1532–38

Bottan S, Schmid Daners M, de Zelicourt D, Fellner N, Poulikakos D, Kurtcuoglu V. 2013. Assessment of intracranial dynamics in hydrocephalus: effects of viscoelasticity on the outcome of infusion tests. *J. Neurosurg.* 119:1511–19

Boulton M, Flessner M, Armstrong D, Mohamed R, Hay J, Johnston M. 1999. Contribution of extracranial lymphatics and arachnoid villi to the clearance of a CSF tracer in the rat. *Am. J. Physiol.* 276:R818–23

Bouma GJ, Muizelaar JP, Bandoh K, Marmarou A. 1992. Blood pressure and intracranial pressure-volume dynamics in severe head injury: relationship with cerebral blood flow. *J. Neurosurg.* 77:15–19

Brisman JL, Pile-Spellman J, Konstas AA. 2012. Clinical utility of quantitative magnetic resonance angiography in the assessment of the underlying pathophysiology in a variety of cerebrovascular disorders. *Eur. J. Radiol.* 81:298–302

Brodbelt A, Stoodley M. 2007. CSF pathways: a review. *Br. J. Neurosurg.* 21:510–20

Bruel BM, Engle MP, Rauck RL, Weber TJ, Kapural L. 2013. Intrathecal drug delivery for control of pain. In *Comprehensive Treatment of Chronic Pain by Medical, Interventional, and Integrative Approaches*, ed. TR Deer, MS Leong, A Buvanendran, V Gordin, PS Kim, et al., pp. 637–48. New York: Springer

Buishas J, Gould IG, Linninger AA. 2014. A computational model of cerebrospinal fluid production and reabsorption driven by Starling forces. *Croat. Med. J.* 55:481–97

Bulat M, Klarica M. 2011. Recent insights into a new hydrodynamics of the cerebrospinal fluid. *Brain Res. Rev.* 65:99–112

Bulat M, Lupret V, Orehković D, Klarica M. 2008. Transventricular and transpial absorption of cerebrospinal fluid into cerebral microvessels. *Coll. Antropol.* 32(Suppl. 1):43–50

Bunck AC, Kröger JR, Jüttner A, Brentrup A, Fiedler B, et al. 2011. Magnetic resonance 4D flow characteristics of cerebrospinal fluid at the craniocervical junction and the cervical spinal canal. *Eur. Radiol.* 21:1788–96

Bunck AC, Kröger JR, Jüttner A, Brentrup A, Fiedler B, et al. 2012. Magnetic resonance 4D flow analysis of cerebrospinal fluid dynamics in Chiari I malformation with and without syringomyelia. *Eur. Radiol.* 22:1860–70

Cahan LD, Bentson JR. 1982. Considerations in the diagnosis and treatment of syringomyelia and the Chiari malformation. *J. Neurosurg.* 57:24–31

Cai J, Chang Z, Wang Z, Segars WP, Yin F-F. 2011. Four-dimensional magnetic resonance imaging (4D-MRI) using image-based respiratory surrogate: a feasibility study. *Med. Phys.* 38:6384–94

Calias P, Banks WA, Begley D, Scarpa M, Dickson P. 2014. Intrathecal delivery of protein therapeutics to the brain: a critical reassessment. *Pharmacol. Ther.* 144:114–22

Calias P, Papisov M, Pan J, Savioli N, Belov VV, et al. 2012. CNS penetration of intrathecal-lumbar idursulfase in the monkey, dog and mouse: implications for neurological outcomes of lysosomal storage disorder. *PLOS ONE* 7:e30341

Carare RO, Bernardes-Silva M, Newman TA, Page AM, Nicoll JAR, et al. 2008. Solutes, but not cells, drain from the brain parenchyma along basement membranes of capillaries and arteries: significance for cerebral amyloid angiopathy and neuroimmunology. *Neuropathol. Appl. Neurobiol.* 34:131–44

Chang HS, Nakagawa H. 2003. Hypothesis on the pathophysiology of syringomyelia based on simulation of cerebrospinal fluid dynamics. *J. Neurol. Neurosurg. Psychiatry* 74:344–47

Charbel FT, Zhao M, Amin-Hanjani S, Hoffman W, Du X, Clark ME. 2004. A patient-specific computer model to predict outcomes of the balloon occlusion test. *J. Neurosurg.* 101:977–88

Cheng S, Fletcher D, Hemley S, Stoodley M, Bilston L. 2014. Effects of fluid structure interaction in a three dimensional model of the spinal subarachnoid space. *J. Biomech.* 47:2826–30

Cheng S, Stoodley MA, Wong J, Hemley S, Fletcher DF, Bilston LE. 2012. The presence of arachnoiditis affects the characteristics of CSF flow in the spinal subarachnoid space: a modelling study. *J. Biomech.* 45:1186–91

Clarke EC, Stoodley MA, Bilston LE. 2013. Changes in temporal flow characteristics of CSF in Chiari malformation Type I with and without syringomyelia: implications for theory of syrinx development. *J. Neurosurg.* 118:1135–40

Cohen B, Voorhees A, Vedel S, Wei T. 2009. Development of a theoretical framework for analyzing cerebrospinal fluid dynamics. *Cerebrospinal Fluid Res.* 6:12

Cousins J, Haughton V. 2009. Motion of the cerebellar tonsils in the foramen magnum during the cardiac cycle. *Am. J. Neuroradiol.* 30:1587–88

Cserr HF. 1971. Physiology of the choroid plexus. *Physiol. Rev.* 51:273–311

Detrembleur C, Plaghki L. 2000. Quantitative assessment of intrathecally administered baclofen in spasticity. *Arch. Phys. Med. Rehabil.* 81:279–84

Dreha-Kulaczewski S, Joseph AA, Merboldt K-D, Ludwig H-C, Gärtner J, Frahm J. 2015. Inspiration is the major regulator of human CSF flow. *J. Neurosci.* 35:2485–91

Ducoffe AR, Konstas AA, Pile-Spellman J, Brisman JL. 2012. Clinical applications of quantitative MRA in neurovascular practice. In *Magnetic Resonance Angiography: Basics to Future*, ed. W Shabana. Rijeka, Croat.: InTech. doi: 10.5772/29874

Dykstra D, Stuckey M, DesLauriers L, Chappuis D, Krach L. 2007. Intrathecal baclofen in the treatment of spasticity. In *Operative Neuromodulation*, ed. DE Sakas, BA Simpson, ES Krames, pp. 163–71. New York: Springer

Edsbagge M, Tisell M, Jacobsson L, Wikkelso C. 2004. Spinal CSF absorption in healthy individuals. *Am. J. Physiol.* 287:R1450–55

Egnor M, Rosiello A, Zheng L. 2001. A model of intracranial pulsations. *Pediatr. Neurosurg.* 35:284–98

Ehlers W, Wagner A. 2013. Constitutive and computational aspects in tumor therapies of multiphasic brain tissue. In *Computer Models in Biomechanics*, ed. GA Holzapfel, E Kuhl, pp. 263–76. New York: Springer

Ehlers W, Wagner A. 2015. Multi-component modelling of human brain tissue: a contribution to the constitutive and computational description of deformation, flow and diffusion processes with application to the invasive drug-delivery problem. *Comput. Methods Biomech. Biomed. Eng.* 18:861–79

Enzmann DR, Pelc NJ. 1992. Brain motion: measurement with phase-contrast MR imaging. *Radiology* 185:653–60

Enzmann DR, Pelc NJ. 1993. Cerebrospinal fluid flow measured by phase-contrast cine MR. *AJNR Am. J. Neuroradiol.* 14:1301–7; discussion 1309–10

Esfahani D, Stevenson M, Moss H, Amin-Hanjani S, Aletich V, et al. 2014. O-011 quantitative MRA is correlated with intravascular pressures before and after venous sinus stenting: implications for treatment and monitoring. *J. Neurointerv. Surg.* 6(Suppl. 1):A6–7

Fernández E, Graña M, Villanúa J. 2011. High resolution segmentation of CSF on phase contrast MRI. In *New Challenges on Bioinspired Applications*, ed. JM Ferrández, JR Álvarez, F de la Paz, FJ Toledo, pp. 96–103. New York: Springer

Freund M, Adwan M, Kooijman H, Heiland S, Thomsen M, et al. 2001. Measurement of CSF flow in the spinal canal using MRI with an optimized MRI protocol: experimental and clinical studies. *RöFo* 173:306–14

Friedman DI, Jacobson DM. 2002. Diagnostic criteria for idiopathic intracranial hypertension. *Neurology* 59:1492–95

Galarza M, Giménez Á, Pellicer O, Valero J, Amigó JM. 2014. New designs of ventricular catheters for hydrocephalus by 3-D computational fluid dynamics. *Childs Nerv. Syst.* 31:37–48

Galarza M, Giménez Á, Valero J, Pellicer OP, Amigó JM. 2013. Computational fluid dynamics of ventricular catheters used for the treatment of hydrocephalus: a 3D analysis. *Childs Nerv. Syst.* 30:105–16

Galarza M, Giménez Á, Valero J, Pellicer O, Martínez-Lage JF, Amigó JM. 2015. Basic cerebrospinal fluid flow patterns in ventricular catheters prototypes. *Childs Nerv. Syst.* 31:873–84

George TM, Higginbotham NH. 2011. Defining the signs and symptoms of Chiari malformation type I with and without syringomyelia. *Neurol. Res.* 33:240–46

Ghaffari M, Hsu C, Linninger A. 2015. *Automatic reconstruction and generation of structured hexahedral mesh for non-planar bifurcations in vascular networks*. Presented at 12th Int. Symp. Process Syst. Eng., 25th Eur. Symp. Comput. Aided Process Eng, Copenhagen

Gould IG, Linninger AA. 2015. Hematocrit distribution and tissue oxygenation in large microcirculatory networks. *Microcirculation* 22:1–18

Gracies J-M, Nance P, Elovic E, McGuire J, Simpson DM. 1997. Traditional pharmacological treatments for spasticity. Part II: general and regional treatments. *Muscle Nerve* 20(Suppl. 6):S92–120

Greitz D. 2004. Radiological assessment of hydrocephalus: new theories and implications for therapy. *Neurosurg. Rev.* 27:145–65

Greitz D, Hannerz J, Rähn T, Bolander H, Ericsson A. 1994. MR imaging of cerebrospinal fluid dynamics in health and disease on the vascular pathogenesis of communicating hydrocephalus and benign intracranial hypertension. *Acta Radiol.* 35:204–11

Gupta S, Poulikakos D, Kurtcuoglu V. 2008. Analytical solution for pulsatile viscous flow in a straight elliptic annulus and application to the motion of the cerebrospinal fluid. *Phys. Fluids* 20:093607

Gupta S, Soellinger M, Boesiger P, Poulikakos D, Kurtcuoglu V. 2009. Three-dimensional computational modeling of subject-specific cerebrospinal fluid flow in the subarachnoid space. *J. Biomech. Eng.* 131:021010

Gupta S, Soellinger M, Grzybowski DM, Boesiger P, Biddiscombe J, et al. 2010. Cerebrospinal fluid dynamics in the human cranial subarachnoid space: an overlooked mediator of cerebral disease. I. Computational model. *J. R. Soc. Interface* 7:1195–204

Hadaczek P, Yamashita Y, Mirek H, Tamas L, Bohn MC, et al. 2006. The "perivascular pump" driven by arterial pulsation is a powerful mechanism for the distribution of therapeutic molecules within the brain. *Mol. Ther.* 14:69–78

Hadzri EA, Osman K, Kadir MRA, Aziz AA. 2011. Computational investigation on CSF flow analysis in the third ventricle and aqueduct of Sylvius. *IIUM Eng. J.* 12:132–41

Haj-Yasein NN, Vindedal GF, Eilert-Olsen M, Gundersen GA, Skare Ø, et al. 2011. Glial-conditional deletion of aquaporin-4 (Aqp4) reduces blood-brain water uptake and confers barrier function on perivascular astrocyte endfeet. *PNAS* 108:17815–20

Hakim S. 1970. Biomechanics of hydrocephalus. *Acta Neurol. Latinoam.* 1(Suppl. 1):169–94

Hakim S, Venegas JG, Burton JD. 1976. The physics of the cranial cavity, hydrocephalus and normal pressure hydrocephalus: mechanical interpretation and mathematical model. *Surg. Neurol.* 5:187–210

Haller FR, Low FN. 1971. The fine structure of the peripheral nerve root sheath in the subarachnoid space in the rat and other laboratory animals. *Am. J. Anat.* 131:1–19

Haslam M, Zamir M. 1998. Pulsatile flow in tubes of elliptic cross sections. *Ann. Biomed. Eng.* 26:780–87
Hebb AO, Cusimano MD. 2001. Idiopathic normal pressure hydrocephalus: a systematic review of diagnosis and outcome. *Neurosurgery* 49:1166–84; discussion 1184–86
Helgeland A, Mardal K-A, Haughton V, Reif BAP. 2014. Numerical simulations of the pulsating flow of cerebrospinal fluid flow in the cervical spinal canal of a Chiari patient. *J. Biomech.* 47:1082–90
Hernández-Mier Y, Blondel WCPM, Daul C, Wolf D, Guillemin F. 2010. Fast construction of panoramic images for cystoscopic exploration. *Comput. Med. Imaging Graph.* 34:579–92
Hettiarachchi HDM, Hsu Y, Harris TJ, Penn R, Linninger AA. 2011. The effect of pulsatile flow on intrathecal drug delivery in the spinal canal. *Ann. Biomed. Eng.* 39:2592–602
Hladky SB, Barrand MA. 2014. Mechanisms of fluid movement into, through and out of the brain: evaluation of the evidence. *Fluids Barriers CNS* 11:26
Hodel J, Besson P, Rahmouni A, Petit E, Lebret A, et al. 2013. 3D mapping of cerebrospinal fluid local volume changes in patients with hydrocephalus treated by surgery: preliminary study. *Eur. Radiol.* 24:136–42
Hodel J, Lebret A, Petit E, Leclerc X, Zins M, et al. 2012. Imaging of the entire cerebrospinal fluid volume with a multistation 3D SPACE MR sequence: feasibility study in patients with hydrocephalus. *Eur. Radiol.* 23:1450–58
Hopkins LN, Bakay L, Kinkel WR, Grand W. 1977. Demonstration of transventricular CSF absorption by computerized tomography. *Acta Neurochir.* 39:151–57
Howden L, Power H, Giddings D, Vloeberghs M. 2011. Three-dimensional cerebrospinal fluid flow within the human central nervous system. *Discrete Contin. Dyn. Syst. B* 15:957–69
Hsu C-Y, Schneller B, Ghaffari M, Alaraj A, Linninger A. 2015. Medical image processing for fully integrated subject specific whole brain mesh generation. *Technologies* 3:126–41
Hsu YB, Hettiarachchi HDM, Zhu DC, Linninger AA. 2012. The frequency and magnitude of cerebrospinal fluid pulsations influence intrathecal drug distribution: key factors for interpatient variability. *Anesth. Analg.* 115:386–94
Hutchings M, Weller RO. 1986. Anatomical relationships of the pia mater to cerebral blood vessels in man. *J. Neurosurg.* 65:316–25
Huyghe JM, Oomens CW, van Campen KH. 1988. Low Reynolds number steady state flow through a branching network of rigid vessels: II. A finite element mixture model. *Biorheology* 26:73–84
Huyghe JM, Oomens CW, van Campen KH, Heethaar RM. 1989. Low Reynolds number steady state flow through a branching network of rigid vessels: I. A mixture theory. *Biorheology* 26:55–71
Hyde ER, Michler C, Lee J, Cookson AN, Chabiniok R, et al. 2013. Parameterisation of multi-scale continuum perfusion models from discrete vascular networks. *Med. Biol. Eng. Comput.* 51:557–70
Iadecola C, Nedergaard M. 2007. Glial regulation of the cerebral microvasculature. *Nat. Neurosci.* 10:1369–76
Iliff JJ, Wang M, Liao Y, Plogg BA, Peng W, et al. 2012. A paravascular pathway facilitates CSF flow through the brain parenchyma and the clearance of interstitial solutes, including amyloid β. *Sci. Transl. Med.* 4:147ra111
Iliff JJ, Wang M, Zeppenfeld DM, Venkataraman A, Plog BA, et al. 2013. Cerebral arterial pulsation drives paravascular CSF-interstitial fluid exchange in the murine brain. *J. Neurosci.* 33:18190–99
Ishii K, Soma T, Shimada K, Oda H, Terashima A, Kawasaki R. 2013. Automatic volumetry of the cerebrospinal fluid space in idiopathic normal pressure hydrocephalus. *Dement. Geriatr. Cogn. Disord. Extra* 3:489–96
Jacobson EE, Fletcher DF, Morgan MK, Johnston IH. 1996. Fluid dynamics of the cerebral aqueduct. *Pediatr. Neurosurg.* 24:229–36
Johnson LN, Krohel GB, Madsen RW, March GA Jr. 1998. The role of weight loss and acetazolamide in the treatment of idiopathic intracranial hypertension (pseudotumor cerebri). *Ophthalmology* 105:2313–17
Johnston M, Zakharov A, Papaiconomou C, Salmasi G, Armstrong D. 2004. Evidence of connections between cerebrospinal fluid and nasal lymphatic vessels in humans, non-human primates and other mammalian species. *Cerebrospinal Fluid Res.* 1:2
Kao Y-H, Guo W-Y, Liou AJ-K, Hsiao Y-H, Chou C-C. 2008. The respiratory modulation of intracranial cerebrospinal fluid pulsation observed on dynamic echo planar images. *Magn. Reson. Imaging* 26:198–205
Kapsalaki E, Svolos P, Tsougos I, Theodorou K, Fezoulidis I, Fountas KN. 2012. Quantification of normal CSF flow through the aqueduct using PC-cine MRI at 3T. *Acta Neurochir. Suppl.* 113:39–42

Karahalios DG, Rekate HL, Khayata MH, Apostolides PJ. 1996. Elevated intracranial venous pressure as a universal mechanism in pseudotumor cerebri of varying etiologies. *Neurology* 46:198–202

Kida S, Pantazis A, Weller RO. 1993. CSF drains directly from the subarachnoid space into nasal lymphatics in the rat: anatomy, histology and immunological significance. *Neuropathol. Appl. Neurobiol.* 19:480–88

Klarica M, Miše B, Vladić A, Radoš M, Orešković D. 2013. "Compensated hyperosmolarity" of cerebrospinal fluid and the development of hydrocephalus. *Neuroscience* 248:278–89

Klarica M, Varda R, Vukić M, Oresković D, Rados M, Bulat M. 2005. Spinal contribution to CSF pressure lowering effect of mannitol in cats. *Acta Neurochir. Suppl.* 95:407–10

Koyanagi I, Houkin K. 2010. Pathogenesis of syringomyelia associated with Chiari type 1 malformation: review of evidences and proposal of a new hypothesis. *Neurosurg. Rev.* 33:271–85

Kurtcuoglu V. 2011. Computational fluid dynamics for the assessment of cerebrospinal fluid flow and its coupling with cerebral blood flow. In *Biomechanics of the Brain*, ed. K Miller, pp. 169–88. New York: Springer

Kurtcuoglu V, Poulikakos D, Ventikos Y. 2005a. Computational modeling of the mechanical behavior of the cerebrospinal fluid system. *J. Biomech. Eng.* 127:264–69

Kurtcuoglu V, Soellinger M, Summers P, Boomsma K, Poulikakos D, et al. 2005b. Reconstruction of cerebrospinal fluid flow in the third ventricle based on MRI data. In *Medical Image Computing and Computer-Assisted Intervention – MICCAI 2005*, ed. JS Duncan, G Gerig, pp. 786–93. New York: Springer

Kurtcuoglu V, Soellinger M, Summers P, Boomsma K, Poulikakos D, et al. 2007. Computational investigation of subject-specific cerebrospinal fluid flow in the third ventricle and aqueduct of Sylvius. *J. Biomech.* 40:1235–45

Kuttler A, Dimke T, Kern S, Helmlinger G, Stanski D, Finelli LA. 2010. Understanding pharmacokinetics using realistic computational models of fluid dynamics: biosimulation of drug distribution within the CSF space for intrathecal drugs. *J. Pharmacokinet. Pharmacodyn.* 37:629–44

Lebret A, Hodel J, Rahmouni A, Decq P, Petit É. 2013. Cerebrospinal fluid volume analysis for hydrocephalus diagnosis and clinical research. *Comput. Med. Imaging Graph.* 37:224–33

Lechtreck K-F, Delmotte P, Robinson ML, Sanderson MJ, Witman GB. 2008. Mutations in Hydin impair ciliary motility in mice. *J. Cell Biol.* 180:633–43

Lee JH, Lee HK, Kim JK, Kim HJ, Park JK, Choi CG. 2004. CSF flow quantification of the cerebral aqueduct in normal volunteers using phase contrast cine MR imaging. *Korean J. Radiol.* 5:81–86

Leeds SE, Kong AK, Wise BL. 1989. Alternative pathways for drainage of cerebrospinal fluid in the canine brain. *Lymphology* 22:144–46

Leliefeld PH, Gooskens RH, Braun KPJ, Ramos LM, Uiterwaal CS, et al. 2009. Longitudinal diffusion-weighted imaging in infants with hydrocephalus: decrease in tissue water diffusion after cerebrospinal fluid diversion. *J. Neurosurg. Pediatr.* 4:56–63

Lemieux L, Hammers A, Mackinnon T, Liu RSN. 2003. Automatic segmentation of the brain and intracranial cerebrospinal fluid in T1-weighted volume MRI scans of the head, and its application to serial cerebral and intracranial volumetry. *Magn. Reson. Med.* 49:872–84

Levine DN. 2000. Ventricular size in pseudotumor cerebri and the theory of impaired CSF absorption. *J. Neurol. Sci.* 177:85–94

Linge SO, Haughton V, Løvgren AE, Mardal KA, Langtangen HP. 2010. CSF flow dynamics at the craniovertebral junction studied with an idealized model of the subarachnoid space and computational flow analysis. *AJNR Am. J. Neuroradiol.* 31:185–92

Linge SO, Mardal K-A, Helgeland A, Heiss JD, Haughton V. 2014. Effect of craniovertebral decompression on CSF dynamics in Chiari malformation type I studied with computational fluid dynamics: laboratory investigation. *J. Neurosurg. Spine* 21:559–64

Linninger AA. 2012. Biomedical systems research: new perspectives opened by quantitative medical imaging. *Comput. Chem. Eng.* 36:1–9

Linninger AA, Basati S, Dawe R, Penn R. 2009a. An impedance sensor to monitor and control cerebral ventricular volume. *Med. Eng. Phys.* 31:838–45

Linninger AA, Gould IG, Marinnan T, Hsu C-Y, Chojecki M, Alaraj A. 2013. Cerebral microcirculation and oxygen tension in the human secondary cortex. *Ann. Biomed. Eng.* 41:2264–84

Linninger AA, Somayaji MR, Mekarski M, Zhang L. 2008. Prediction of convection-enhanced drug delivery to the human brain. *J. Theor. Biol.* 250:125–38
Linninger AA, Sweetman B, Penn R. 2009b. Normal and hydrocephalic brain dynamics: the role of reduced cerebrospinal fluid reabsorption in ventricular enlargement. *Ann. Biomed. Eng.* 37:1434–47
Linninger AA, Tsakiris C, Zhu DC, Xenos M, Roycewicz P, et al. 2005. Pulsatile cerebrospinal fluid dynamics in the human brain. *IEEE Trans. Biomed. Eng.* 52:557–65
Linninger AA, Xenos M, Sweetman B, Ponkshe S, Guo X, Penn R. 2009c. A mathematical model of blood, cerebrospinal fluid and brain dynamics. *J. Math. Biol.* 59:729–59
Linninger AA, Xenos M, Zhu DC, Somayaji MR, Kondapalli S, Penn RD. 2007. Cerebrospinal fluid flow in the normal and hydrocephalic human brain. *IEEE Trans. Biomed. Eng.* 54:291–302
Lorenzo AV, Page LK, Watters GV. 2015. Relationship between cerebrospinal fluid formation, absorption and pressure in human hydrocephalus. *Brain* 93:679–92
Loth F, Yardimci MA, Alperin N. 2000. Hydrodynamic modeling of cerebrospinal fluid motion within the spinal cavity. *J. Biomech. Eng.* 123:71–79
Louveau A, Smirnov I, Keyes TJ, Eccles JD, Rouhani SJ, et al. 2015. Structural and functional features of central nervous system lymphatic vessels. *Nature* 523:337–41
MacAulay N, Zeuthen T. 2010. Water transport between CNS compartments: contributions of aquaporins and cotransporters. *Neuroscience* 168:941–56
Mackley MR, Ni X. 1991. Mixing and dispersion in a baffled tube for steady laminar and pulsatile flow. *Chem. Eng. Sci.* 46:3139–51
Mao B, Zhang H, Zhao K, Sun H, Shan Y. 2010. Cerebrospinal fluid absorption disorder of arachnoid villi in a canine model of hydrocephalus. *Neurol. India* 58:371–76
Markl M, Chan FP, Alley MT, Wedding KL, Draney MT, et al. 2003. Time-resolved three-dimensional phase-contrast MRI. *J. Magn. Reson. Imaging* 17:499–506
Marmarou A, Shulman K, LaMorgese J. 1975. Compartmental analysis of compliance and outflow resistance of the cerebrospinal fluid system. *J. Neurosurg.* 43:523–34
Martin BA, Kalata W, Loth F, Royston TJ, Oshinski JN. 2005. Syringomyelia hydrodynamics: an in vitro study based on in vivo measurements. *J. Biomech. Eng.* 127:1110–20
Martin BA, Labuda R, Royston TJ, Oshinski JN, Iskandar B, Loth F. 2010. Spinal subarachnoid space pressure measurements in an in vitro spinal stenosis model: implications on syringomyelia theories. *J. Biomech. Eng.* 132:111007
Martin BA, Loth F. 2009. The influence of coughing on cerebrospinal fluid pressure in an in vitro syringomyelia model with spinal subarachnoid space stenosis. *Cerebrospinal Fluid Res.* 6:17
Mbonane SS, Andronikou S. 2013. Interpretation and value of MR CSF flow studies for paediatric neurosurgery. *South Afr. J. Radiol.* 17:26–29
McGirt MJ, Nimjee SM, Floyd J, Bulsara KR, George TM. 2005. Correlation of cerebrospinal fluid flow dynamics and headache in Chiari I malformation. *Neurosurgery* 56:716–21
Milhorat TH. 1969. Choroid plexus and cerebrospinal fluid production. *Science* 166:1514–16
Milhorat TH, Hammock MK, Fenstermacher JD, Levin VA. 1971. Cerebrospinal fluid production by the choroid plexus and brain. *Science* 173:330–32
Narsilio G, Shen X, Wang H, Smith D, Egan G. 2008. Hydrocephalus: a realistic porous-media model with geometry based on neuroimaging. In *Advances in Cognitive Neurodynamics ICCN 2007*, ed. R Wang, E Shen, F Gu, pp. 565–69. New York: Springer
Nash J, Cheng JS, Meyer GA, Remier BF. 2001. Chiari type I malformation: overview of diagnosis and treatment. *WMJ* 101:35–40
Navarro R, Feroze A, Choudhri O, Lober R, Khan N, Steinberg G. 2014. E-014 changes in posterior circulation arterial flows after revascularization surgery in moyamoya disease: a quantitative MRI study. *J. Neurointerv. Surg.* 6(Suppl. 1):A44
Nedergaard M, Ransom B, Goldman SA. 2003. New roles for astrocytes: redefining the functional architecture of the brain. *Trends Neurosci.* 26:523–30
Nitz WR, Bradley WG, Watanabe AS, Lee RR, Burgoyne B, et al. 1992. Flow dynamics of cerebrospinal fluid: assessment with phase-contrast velocity MR imaging performed with retrospective cardiac gating. *Radiology* 183:395–405

Orešković D, Klarica M. 2011. Development of hydrocephalus and classical hypothesis of cerebrospinal fluid hydrodynamics: facts and illusions. *Prog. Neurobiol.* 94:238–58

Özsarlak Ö, Goethem JWV, Maes M, Parizel PM. 2004. MR angiography of the intracranial vessels: technical aspects and clinical applications. *Neuroradiology* 46:955–72

Pahlavian HS, Yiallourou T, Tubbs RS, Bunck AC, Loth F, et al. 2014. The impact of spinal cord nerve roots and denticulate ligaments on cerebrospinal fluid dynamics in the cervical spine. *PLOS ONE* 9:e91888

Pandey A, Pati UC. 2014. A novel technique for mosaicing of medical images. In *2014 Annu. IEEE India Conf.* (*INDICON*), pp. 1–5. New York: IEEE

Papadopoulos MC, Verkman AS. 2013. Aquaporin water channels in the nervous system. *Nat. Rev. Neurosci.* 14:265–77

Papisov MI, Belov VV, Fischman AJ, Belova E, Titus J, et al. 2012. Delivery of proteins to CNS as seen and measured by positron emission tomography. *Drug Deliv. Transl. Res.* 2:201–9

Papisov MI, Belov VV, Gannon KS. 2013. Physiology of the intrathecal bolus: the leptomeningeal route for macromolecule and particle delivery to CNS. *Mol. Pharm.* 10:1522–32

Penn RD, Bacus JW. 1984. The brain as a sponge: a computed tomographic look at Hakim's hypothesis. *Neurosurgery* 14:670–75

Penn RD, Basati S, Sweetman B, Guo X, Linninger AA. 2011. Ventricle wall movements and cerebrospinal fluid flow in hydrocephalus. *J. Neurosurg.* 115:159–64

Penn RD, Kurtz D. 1977. Cerebral edema, mass effects, and regional blood volume in man. *J. Neurosurg.* 46:282–89

Penn RD, Lee MC, Linninger AA, Miesel K, Lu SN, Stylos L. 2009. Pressure gradients in the brain in an experimental model of hydrocephalus. *Collections* 116:1069–75

Petrella G, Czosnyka M, Keong N, Pickard JD, Czosnyka Z. 2008. How does CSF dynamics change after shunting? *Acta Neurol. Scand.* 118:182–88

Piot E, Tavoularis S. 2011. Gap instability of laminar flows in eccentric annular channels. *Nucl. Eng. Des.* 241:4615–20

Pohl DM, Rockstroh G, Rückriem S, Mehrholz J, Pause M, et al. 2003. Time course of the effect of a bolus dose of intrathecal baclofen on severe cerebral spasticity. *J. Neurol.* 250:1195–200

Prabhakaran S, Warrior L, Wells KR, Jhaveri MD, Chen M, Lopes DK. 2009. The utility of quantitative magnetic resonance angiography in the assessment of intracranial in-stent stenosis. *Stroke* 40:991–93

Prager J, Deer T, Levy R, Bruel B, Buchser E, et al. 2014. Best practices for intrathecal drug delivery for pain. *Neuromodul. Technol. Neural Interface* 17:354–72

Qvarlander S, Malm J, Eklund A. 2013. CSF dynamic analysis of a predictive pulsatility-based infusion test for normal pressure hydrocephalus. *Med. Biol. Eng. Comput.* 52:75–85

Ragheb AS, Mohammed FF, El-Anwar MW. 2014. Cerebrospinal fluid rhinorrhea: diagnostic role of gadolinium enhanced MR cisternography. *Egypt. J. Radiol. Nucl. Med.* 45:841–47

Raphael JH, Duarte RV, Southall JL, Nightingale P, Kitas GD. 2013. Randomised, double-blind controlled trial by dose reduction of implanted intrathecal morphine delivery in chronic non-cancer pain. *BMJ Open* 3:e003061

Reimer P, Boos M. 1999. Phase-contrast MR angiography of peripheral arteries: technique and clinical application. *Eur. Radiol.* 9:122–27

Reina MA, Casasola ODL, Villanueva MC, Lopez A, Maches F, De Andrés JA. 2004. Ultrastructural findings in human spinal pia mater in relation to subarachnoid anesthesia. *Anesth. Analg.* 98:1479–85

Reina MA, De Andrés JA, Hadzic A, Prats-Galino A, Sala-Blanch X, van Zundert AAJ, eds. 2015. *Atlas of Functional Anatomy for Regional Anesthesia and Pain Medicine: Human Structure, Ultrastructure and 3D Reconstruction Images*. New York: Springer

Reina MA, de Leon Casasola O, López A, De Andrés JA, Mora M, Fernández A. 2002a. The origin of the spinal subdural space: ultrastructure findings. *Anesth. Analg.* 94:991–95

Reina MA, López A, Machés F, de Leon Casasola O, De Andrés JA. 2002b. Electron microscopy and the expansion of regional anesthesia knowledge. *Tech. Reg. Anesth. Pain Manag.* 6:165–71

Roldan A, Wieben O, Haughton V, Osswald T, Chesler N. 2009. Characterization of CSF hydrodynamics in the presence and absence of tonsillar ectopia by means of computational flow analysis. *AJNR Am. J. Neuroradiol.* 30:941–46

Ross MR, Pelc NJ, Enzmann DR. 1993. Qualitative phase contrast MRA in the normal and abnormal circle of Willis. *Am. J. Neuroradiol.* 14:19–25

Rutkowska G, Haughton V, Linge S, Mardal K-A. 2012. Patient-specific 3D simulation of cyclic CSF flow at the craniocervical region. *AJNR Am. J. Neuroradiol.* 33:1756–62

Sæhle T, Eide PK. 2015. Association between ventricular volume measures and pulsatile and static intracranial pressure scores in non-communicating hydrocephalus. *J. Neurol. Sci.* 350:33–39

Sakka L, Coll G, Chazal J. 2011. Anatomy and physiology of cerebrospinal fluid. *Eur. Ann. Otorhinolaryngol. Head Neck Dis.* 128:309–16

Schley D, Carare-Nnadi R, Please CP, Perry VH, Weller RO. 2006. Mechanisms to explain the reverse perivascular transport of solutes out of the brain. *J. Theor. Biol.* 238:962–74

Schroth G, Klose U. 1992. Cerebrospinal fluid flow. *Neuroradiology* 35:10–15

Shah S, Haughton V, del Río AM. 2011. CSF flow through the upper cervical spinal canal in Chiari I malformation. *Am. J. Neuroradiol.* 32:1149–53

Shapiro K, Marmarou A, Shulman K. 1980. Characterization of clinical CSF dynamics and neural axis compliance using the pressure-volume index: I. The normal pressure-volume index. *Ann. Neurol.* 7:508–14

Shyy W, Udaykumar HS, Rao MM, Smith RW. 2012. *Computational Fluid Dynamics with Moving Boundaries*. Mineola, NY: Dover

Sindhwani N, Ivanchenko O, Lueshen E, Prem K, Linninger AA. 2011. Methods for determining agent concentration profiles in agarose gel during convection-enhanced delivery. *IEEE Trans. Biomed. Eng.* 58:626–32

Sivaloganathan S, Tenti G, Drake JM. 1998. Mathematical pressure volume models of the cerebrospinal fluid. *Appl. Math. Comput.* 94:243–66

Siyahhan B, Knobloch V, de Zélicourt D, Asgari M, Schmid Daners M, et al. 2014. Flow induced by ependymal cilia dominates near-wall cerebrospinal fluid dynamics in the lateral ventricles. *J. R. Soc. Interface* 11:20131189

Smith JH, Humphrey JAC. 2007. Interstitial transport and transvascular fluid exchange during infusion into brain and tumor tissue. *Microvasc. Res.* 73:58–73

Somayaji MR, Xenos M, Zhang L, Mekarski M, Linninger AA. 2008. Systematic design of drug delivery therapies. *Comput. Chem. Eng.* 32:89–98

Sorek S, Bear J, Karni Z. 1988a. A non-steady compartmental flow model of the cerebrovascular system. *J. Biomech.* 21:695–704

Sorek S, Bear J, Karni Z. 1988b. Intracranial compartmental pulse-wave simulation. *Math. Biosci.* 89:149–59

Sorek S, Bear J, Karni Z. 1989. Resistances and compliances of a compartmental model of the cerebrovascular system. *Ann. Biomed. Eng.* 17:1–12

Stalder AF, Russe MF, Frydrychowicz A, Bock J, Hennig J, Markl M. 2008. Quantitative 2D and 3D phase contrast MRI: optimized analysis of blood flow and vessel wall parameters. *Magn. Reson. Med.* 60:1218–31

Stevens SA, Lakin WD. 2000. Local compliance effects on the global pressure-volume relationship in models of intracranial pressure dynamics. *Math. Comput. Model. Dyn. Syst.* 6:445–65

Stockman HW. 2005. Effect of anatomical fine structure on the flow of cerebrospinal fluid in the spinal subarachnoid space. *J. Biomech. Eng.* 128:106–14

Stockman HW. 2007. Effect of anatomical fine structure on the dispersion of solutes in the spinal subarachnoid space. *J. Biomech. Eng.* 129:666–75

Struck AF, Haughton VM. 2009. Idiopathic syringomyelia: phase-contrast MR of cerebrospinal fluid flow dynamics at level of foramen magnum. *Radiology* 253:184–90

Sundström P, Wåhlin A, Ambarki K, Birgander R, Eklund A, Malm J. 2010. Venous and cerebrospinal fluid flow in multiple sclerosis: a case-control study. *Ann. Neurol.* 68:255–59

Sweetman B, Linninger AA. 2010. Cerebrospinal fluid flow dynamics in the central nervous system. *Ann. Biomed. Eng.* 39:484–96

Sweetman B, Xenos M, Zitella L, Linninger AA. 2011. Three-dimensional computational prediction of cerebrospinal fluid flow in the human brain. *Comput. Biol. Med.* 41:67–75

Tangen KM, Hsu Y, Zhu DC, Linninger AA. 2015. CNS wide simulation of flow resistance and drug transport due to spinal microanatomy. *J. Biomech.* 48:2144–54

Taviani V, Patterson AJ, Worters P, Sutcliffe MPF, Graves MJ, Gillard JH. 2010. Accuracy of phase contrast, black-blood, and bright-blood pulse sequences for measuring compliance and distensibility coefficients in a human-tissue mimicking phantom. *J. Magn. Reson. Imaging* 31:160–67

Towns J, Cockerill T, Dahan M, Foster I, Gaither K, et al. 2014. XSEDE: accelerating scientific discovery. *Comput. Sci. Eng.* 16:62–74

Tully B, Ventikos Y. 2009. Coupling poroelasticity and CFD for cerebrospinal fluid hydrodynamics. *IEEE Trans. Biomed. Eng.* 56:1644–51

Tumani H, Teunissen C, Süssmuth S, Otto M, Ludolph AC, Brettschneider J. 2008. Cerebrospinal fluid biomarkers of neurodegeneration in chronic neurological diseases. *Expert Rev. Mol. Diagn.* 8:479–94

Ucar M, Tokgoz N, Damar C, Alimli AG, Oncu F. 2015. Diagnostic performance of heavily T2-weighted techniques in obstructive hydrocephalus: comparison study of two different 3D heavily T2-weighted and conventional T2-weighted sequences. *Jpn. J. Radiol.* 33:94–101

Uftring SJ, Chu D, Alperin N, Levin DN. 2000. The mechanical state of intracranial tissues in elderly subjects studied by imaging CSF and brain pulsations. *Magn. Reson. Imaging* 18:991–96

Van Schaeybroeck P, Nuttin B, Lagae L, Schrijvers E, Borghgraef C, Feys P. 2000. Intrathecal baclofen for intractable cerebral spasticity: a prospective placebo-controlled, double-blind study. *Neurosurgery* 46:603–9; discussion 609–12

Vanneste JAL. 2000. Diagnosis and management of normal-pressure hydrocephalus. *J. Neurol.* 247:5–14

Vanopdenbosch LJ, Dedeken P, Casselman JW, Vlaminck SAPA. 2011. MRI with intrathecal gadolinium to detect a CSF leak: a prospective open-label cohort study. *J. Neurol. Neurosurg. Psychiatry* 82:456–58

Vardakis JC, Tully BJ, Ventikos Y. 2013. Multicompartmental poroelasticity as a platform for the integrative modeling of water transport in the brain. In *Computer Models in Biomechanics*, ed. GA Holzapfel, E Kuhl, pp. 305–16. New York: Springer

Wachinger C, Glocker B, Zeltner J, Paragios N, Komodakis N, et al. 2008. Deformable mosaicing for whole-body MRI. In *Medical Image Computing and Computer-Assisted Intervention – MICCAI 2008*, ed. D Metaxas, L Axel, G Fichtinger, G Székely, pp. 113–21. New York: Springer

Wagner A, Ehlers W. 2010. Continuum-mechanical analysis of human brain tissue. *Proc. Appl. Math. Mech.* 10:99–100

Wagner A, Ehlers W. 2012. Multiphasic modelling of human brain tissue for intracranial drug-infusion studies. *Proc. Appl. Math. Mech.* 12:107–10

Wagshul ME, Chen JJ, Egnor MR, McCormack EJ, Roche PE. 2006. Amplitude and phase of cerebrospinal fluid pulsations: experimental studies and review of the literature. *J. Neurosurg.* 104:810–19

Wagshul ME, Eide PK, Madsen JR. 2011. The pulsating brain: a review of experimental and clinical studies of intracranial pulsatility. *Fluids Barriers CNS* 8:5

Wagshul ME, Johnston M. 2013. The brain and the lymphatic system. In *Immunology of the Lymphatic System*, ed. L Santambrogio, pp. 143–64. New York: Springer

Weller RO, Kida S, Zhang E-T. 1992. Pathways of fluid drainage from the brain: morphological aspects and immunological significance in rat and man. *Brain Pathol.* 2:277–84

Wentland AL, Wieben O, Korosec FR, Haughton VM. 2010. Accuracy and reproducibility of phase-contrast MR imaging measurements for CSF flow. *Am. J. Neuroradiol.* 31:1331–36

Williams B. 1981. Simultaneous cerebral and spinal fluid pressure recordings. I. Technique, physiology, and normal results. *Acta Neurochir.* 58:167–85

Williams MA, McAllister JP, Walker ML, Kranz DA, Bergsneider M, et al. 2007. Priorities for hydrocephalus research: report from a National Institutes of Health–sponsored workshop. *J. Neurosurg.* 107:345–57

Yada K, Nakagawa Y, Tsuru M. 1973. Circulatory disturbance of the venous system during experimental intracranial hypertension. *J. Neurosurg.* 39:723–29

Yaksh TL, Hassenbusch S, Burchiel K, Hildebrand KR, Page LM, Coffey RJ. 2002. Inflammatory masses associated with intrathecal drug infusion: a review of preclinical evidence and human data. *Pain Med.* 3:300–12

Yaksh TL, Noueihed R. 1985. The physiology and pharmacology of spinal opiates. *Annu. Rev. Pharmacol. Toxicol.* 25:433–62

Yamada S, Miyazaki M, Yamashita Y, Ouyang C, Yui M, et al. 2013. Influence of respiration on cerebrospinal fluid movement using magnetic resonance spin labeling. *Fluids Barriers CNS* 10:36

Yang L, Kress BT, Weber HJ, Thiyagarajan M, Wang B, et al. 2013. Evaluating glymphatic pathway function utilizing clinically relevant intrathecal infusion of CSF tracer. *J. Transl. Med.* 11:107

Yiallourou TI, Kröger JR, Stergiopulos N, Maintz D, Martin BA, Bunck AC. 2012. Comparison of 4D phase-contrast MRI flow measurements to computational fluid dynamics simulations of cerebrospinal fluid motion in the cervical spine. *PLOS ONE* 7:e52284

Yoshida K, Takahashi H, Saijo M, Ueguchi T, Tanaka H, et al. 2009. Phase-contrast MR studies of CSF flow rate in the cerebral aqueduct and cervical subarachnoid space with correlation-based segmentation. *Magn. Reson. Med. Sci.* 8:91–100

Zagzoule M, Marc-Vergnes JP. 1986. A global mathematical model of the cerebral circulation in man. *J. Biomech.* 19:1015–22

Zakharov A, Papaiconomou C, Djenic J, Midha R, Johnston M. 2003. Lymphatic cerebrospinal fluid absorption pathways in neonatal sheep revealed by subarachnoid injection of Microfil. *Neuropathol. Appl. Neurobiol.* 29:563–73

Zeuthen T. 2010. Water-transporting proteins. *J. Membr. Biol.* 234:57–73

Zhang ET, Inman CB, Weller RO. 1990. Interrelationships of the pia mater and the perivascular (Virchow-Robin) spaces in the human cerebrum. *J. Anat.* 170:111–23

Zhao M, Amin-Hanjani S, Ruland S, Curcio AP, Ostergren L, Charbel FT. 2007. Regional cerebral blood flow using quantitative MR angiography. *Am. J. Neuroradiol.* 28:1470–73

Zhu DC, Xenos M, Linninger AA, Penn RD. 2006. Dynamics of lateral ventricle and cerebrospinal fluid in normal and hydrocephalic brains. *J. Magn. Reson. Imaging* 24:756–70

Zimmerman RD, Fleming CA, Lee BC, Saint-Louis LA, Deck MD. 1986. Periventricular hyperintensity as seen by magnetic resonance: prevalence and significance. *AJR Am. J. Roentgenol.* 146:443–50